energies

MDPI

Article

Energy Management Systems' Modeling and Optimization in Hybrid Electric Vehicles

Yavuz Eray Altun * and Osman Akın Kutlar

Faculty of Mechanical Engineering, Istanbul Technical University, Istanbul 34467, Turkey; kutlar@itu.edu.tr
* Correspondence: y.erayaltun@gmail.com

Abstract: Optimization studies for the energy management systems of hybrid electric powertrains have critical importance as an effective measure for vehicle manufacturers to reduce greenhouse gas emissions and fuel consumption due to increasingly stringent emission regulations in the automotive industry, strict fuel economy legislation, continuously rising oil prices, and increasing consumer awareness of global warming and environmental pollution. In this study, firstly, the mathematical model of the powertrain and the rule-based energy management system of the vehicle with a power-split hybrid electric vehicle configuration are developed in the Matlab/Simulink environment and verified with real test data from the vehicle dynamometer for the UDDS drive cycle. In this way, a realistic virtual test platform has been developed where the simulation results of the energy management systems based on discrete dynamic programming and Pontryagin's minimum principle optimization can be used to train the artificial neural network-based energy management algorithms for hybrid electric vehicles. The average fuel consumption in relation to the break specific fuel consumption of the internal combustion engine and the total electrical energy consumption of the battery in relation to the operating efficiency of the electrical machines, obtained by comparing the simulation results at the initial battery charging conditions of the vehicle using different driving cycles, will be analyzed and the advantages of the different energy management techniques used will be evaluated.

Keywords: energy management systems; hybrid electric vehicles; discrete dynamic programming; Pontryagin's minimum principle; artificial neural networks; rule-based control

check for updates

Citation: Altun, Y.E.; Kutlar, O.A. Energy Management Systems' Modeling and Optimization in Hybrid Electric Vehicles. *Energies* **2024**, *17*, 1696. https://doi.org/10.3390/en17071696

Academic Editor: Jesus C. Hernandez

Received: 13 February 2024
Revised: 15 March 2024
Accepted: 29 March 2024
Published: 2 April 2024

Copyright: © 2024 by the authors. Licensee MDPI, Basel, Switzerland. This article is an open access article distributed under the terms and conditions of the Creative Commons Attribution (CC BY) license (https://creativecommons.org/licenses/by/4.0/).

1. Introduction

Since the industrial revolution, increased reliance on and demand for fossil fuels has led to a rapid increase in global carbon dioxide emissions, contributing to global warming, and transport emissions are the second largest source after industrial emissions [1]. According to studies by the EU and other sources, about 28% of all carbon dioxide (CO_2) emissions are attributed to the transport sector, and road transport is responsible for more than 70% of these emissions [2]. The transport sector accounts for 28% of the total energy use in the US and 5% globally [3]. Rising fuel prices and concerns about global warming have been the main drivers in the automotive industry towards hybrid electric vehicles, a development process towards advanced powertrains [4]. HEVs have the potential to reduce fuel consumption and emissions significantly, while meeting vehicle power demands and maintaining satisfactory vehicle performance [5–7]. HEVs combine the use of an engine and electric motors, resulting in better fuel efficiency and lower emissions, further reducing dependence on fossil fuels and environmental impact [8,9]. The power required by the vehicle at any time can be provided by one or a combination of these energy sources [10]. The electric motor supports the engine by reducing the workload and optimizing fuel consumption, resulting in lower fuel consumption and greenhouse gas emissions [7,11–13]. It also improves fuel and energy efficiency as the kinetic energy generated during regenerative braking can be recovered and used to power the vehicle in the subsequent process [14].

The electric motor in the system can produce high torque immediately, and it improves acceleration and overall driving performance [2].

The control performance of HEVs is determined by the power distribution between multiple power sources via energy management systems [15,16]. Torque distribution and optimal hybrid driving mode selection are critical to achieving improved fuel economy and reduced emissions [6,15–17]. Energy management system optimization for power-split hybrid electric vehicle configurations has been increasingly attracting researchers' attentions because of its torque split ability based on different drive conditions to improve fuel economy and energy consumption by optimizing the usage of different power sources in the vehicle.

Hwang et al. developed a particle swarm optimization (PSO) technique for control applications to reduce fuel consumption while the vehicle still meets the dynamic performance requirements [1]. Galan et al. introduced a neural network (NN)-based method to predict fuel economy and emissions of the power-split HEV accurately by using real world data in order to determine optimal powertrain control parameters [3]. Tribioli et al. analyzed and compared the performance of the power-split vehicle configuration by using Pontryagin's minimum principle (PMP) with a charge-depleting–charge-sustaining (CD/CS) strategy [4]. Yuan et al. introduced a comparative study by using dynamic programming (DP) and Pontryagin's minimum principle (PMP)-based energy management methods for parallel HEVs [5]. Surresh et al. developed a power-split HEV model configuration and validated it with experimental data from different drive cycles in order to analyze and optimize fuel consumption in the vehicle [7]. Barmaki et al. developed a fuzzy logic (FL)-based controller which is optimized with the genetic algorithm in order to improve fuel efficiency and emissions reduction for PHEVs [9]. Millo et al. introduced equivalent consumption minimization strategy (ECMS)-based local optimization to reduce CO_2 emissions for complex HEV configurations and evaluated the potential of heuristic control techniques [10]. Saurabh et al. modeled and validated an artificial neural network (ANN)-based supervisory controller in charge-sustaining mode operations to predict the net energy consumption in different drive cycles [15]. Liu et al. developed a genetic algorithm (GA)-based energy management strategy for the power-split HEV configuration and compared total energy consumption with the CD/CS method in different drive cycles. He also proposed that artificial intelligence (AI) is expected to achieve better performance in the energy management of PHEVs in the future [16].

However, the aforementioned studies mainly focused on offline optimization or prediction of the control parameters to enhance the energy efficiency and emissions of HEVs. Proposed global optimization methods are not suitable for real-time applications due to computational loads. Few studies only introduced optimization methods for real-time applications.

The main objective of this study is to develop mathematical models of a hybrid electric vehicle with a power-split configuration and use these validated models to design different energy management systems to ensure the most efficient hybrid driving mode selection through optimization of the operating efficiency of the engine and electric motor. The objective is to develop optimization-based energy management strategies based on discrete dynamic programming (DDP), Pontryagin's minimum principle (PMP), and artificial neural networks (ANNs) trained with their simulation results; to reduce the average fuel consumption and the amount of electrical energy drawn from the battery in different driving cycles; and to compare their superiority over the traditional rule-based management systems which requires intensive calibration and vehicle testing. In the first stage, the mathematical model of a hybrid electric vehicle with a rule-based energy management system was created in the Matlab/Simulink environment and validated with dynamometer test data for the UDDS driving cycle on charge-sustaining (CS) mode to obtain a realistic virtual test platform to analyze the simulation results. After that, the results of global optimization-based algorithms based on DDP and PMP, which require the driving cycle information and cannot be applied in real-world conditions due to the high computational

load, were obtained and their superiority over the rule-based control method was analyzed. Then, by using the simulation results of these optimization-based algorithms, learning-based ANN structures, which do not require predefined driving cycle information, are trained offline for different driving cycles and initial conditions, and a deep learning-based hybrid mode selection algorithm is obtained and compared with the rule-based energy management strategy, which is often used as a reference point in the literature, for different driving cycles and initial conditions, and the superiority of the ANN method is investigated.

The main contributions of this paper mainly include the following aspects: (1) The development of a validated virtual test bench environment for the simulation of different energy management systems. (2) The development of PMP- and DP-based algorithms to optimize control parameters of power-split hybrid vehicles in order to reduce energy consumption for defined drive cycles as an offline simulation. (2) Based on the results of the DDP and PMP optimization algorithms, ANN-based energy management systems with three different optimization methods (Levenberg–Marquart, Bayesian Regulation, and Scaled Conjugate Gradient) are developed to improve the fuel economy and battery electrical energy consumption which could be used for real-time applications.

The remainder of this paper is organized as follows: Section 2 presents hybrid electric vehicle configurations, vehicle operation modes, and a detailed description of the mathematical modeling of the components such as the internal combustion engine, electric motors, transmission, battery, and the vehicle dynamic system. Also, driver model and characteristics of the drive cycles used in the simulations are explained in this section. In Section 3, hybrid electric vehicle model validation results in the UDSS driving cycle are presented and analyzed based on the vehicle dynameter data to present the high maturity of the simulation models. In Section 4, classifications and the main objectives of the energy management systems are explained. In this section, control and optimization techniques which will be used in the power-split HEV simulations are explained with their advantages and disadvantages. Also, detailed mathematical modeling of the optimization methods used for simulations are described. Section 5 presents the simulation results and discusses and describes the qualitative and quantitative findings in different drive cycles for the energy management systems developed. Section 6 draws the conclusions based on the obtained simulation results.

2. Hybrid Electric Vehicle Modeling

2.1. Hybrid Electric Vehicle Configuration

In this study, a power-split hybrid electric vehicle configuration is used in the simulation and modeling phase. In this configuration, the internal combustion engine and two electric machines are connected to a planetary gear set, thus allowing these components to work together or independently to power the wheels [18–20]. Clutches can provide the reaction torque by holding the ring gear of each planetary gear set. When the clutch (C1) and one-way clutch (OWC) are engaged, both electric motors can provide maximum output torque as a dual-motor electric drive. The engine power is transmitted through the drive shaft via the mechanically coupled ring gear, while the rest of the power is converted into electric power by a gear set for charging the battery [2]. The automatic transmission consists of two different planetary gear sets (PGS1-PGS2) and has six different gear ratios. The engine can be disconnected from the system using the one-way clutch. The C1 clutch controls the connection of MGA and the C2 clutch controls the connection of MGB to the system [21]. In the modeling phase, the hybrid power-split configuration parameters of the second-generation Chevrolet Volt vehicle are used as seen in Figure 1 [22,23].

Depending on the driving conditions, this configuration allows for various operating modes such as pure electric mode, series hybrid mode, and parallel hybrid mode according to power distribution [9,13,17,20,24–26]. It offers advantages such as improved fuel efficiency, performance, and reduced emissions by providing more flexibility in power management and optimization under different driving conditions [14,27–29].

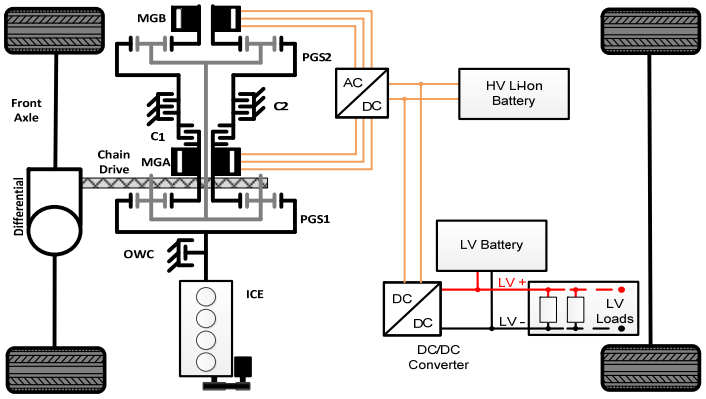

Figure 1. Power-split hybrid electric vehicle configuration.

2.2. Hybrid Electric Vehicle Parameters

The detailed modeling performed during the development phases of hybrid electric vehicle control systems focuses mainly on individual powertrain components such as the engine, electric machines, transmission, and battery and aims to provide detailed information about the specific characteristics of the modeled component as shown in Table A1 [10,15]. The vehicle road load curve and battery cell characteristics are shown in Figure 2 [21,22,30].

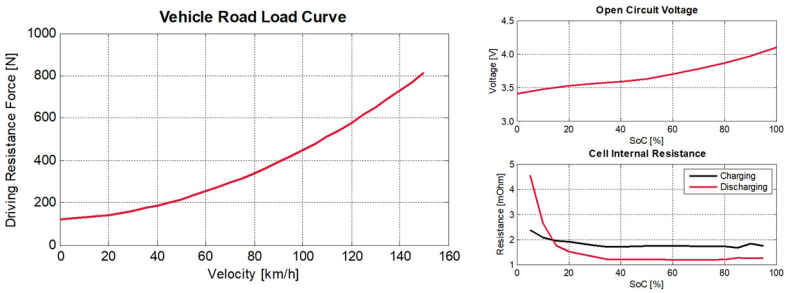

Figure 2. Vehicle road load curve and battery open cycle voltage—cell internal resistance.

The efficiency map of the electric machines MGA and MGB and the BSFC map of the engine are shown in Figure 3 [7,30].

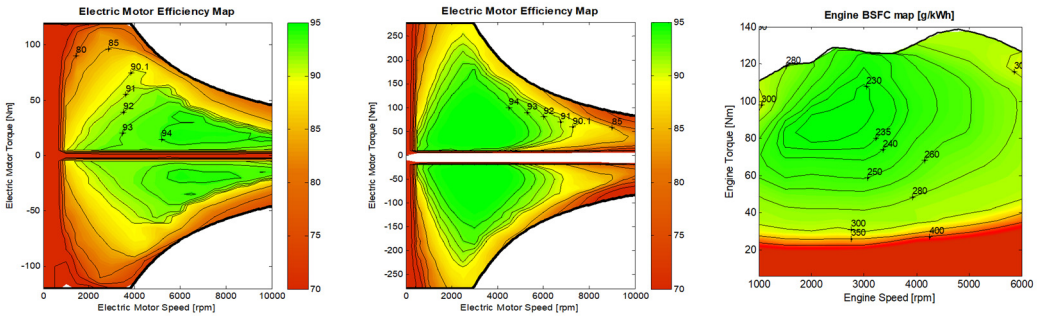

Figure 3. Electric motor/generator MGA and MGB efficiencies and internal combustion engine BSFC.

2.3. Hybrid Electric Vehicle Operating Modes

Hybrid powertrains with multiple power sources provide a large design space for the system and increase the complexity of the control algorithm [2]. The power split hybrid electric vehicle configuration requires the engine operating points to be controlled within an appropriate range by controlling the torque split between the mechanical and electrical power sources according to the vehicle's power demand [31,32]. The main challenge of a power management strategy is to distribute power in the optimal mode to achieve

the desired performance within the system constraints [2]. The hybrid electric vehicle configuration used has five operating modes, including two charge-depletion (CD) modes (EV1 and EV2), three charge-sustaining (CS) modes, low extended range (LERM), fixed gear extended range (FERM), and high extended range (HERM), and the hybrid vehicle energy management system selects the vehicle operating mode to achieve the best energy conversion efficiency while meeting its constraints such as driving emissions [15]. System operating characteristics are shown in Figure 4 [30,31].

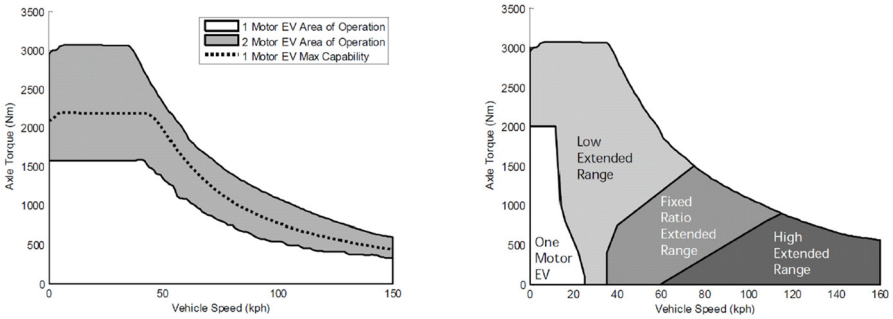

Figure 4. Hybrid electric vehicle driving modes.

Depending on the level of system torque demand, the electric drive modes can be activated as required by the HCU. The single-motor electric drive mode (EV1) is an all-electric mode in which the MGB provides the only power to drive the vehicle as required by the driver, with the ICE and MGA switched off [31]. During this mode, the C2 clutch is closed and the C1 clutch is open, and as the OWC (one-way clutch) is disengaged, the MGB unit is activated for regenerative braking as well as driving the vehicle [15]. This mode is used for low-load operating requirements [7]. The two-motor electric drive (EV2) mode is used to meet the short-term demand for wheel torque by using both electric motors when the MGB reaches its maximum torque limits in EV1 mode [31]. The EV2 mode is an all-electric mode where the engine is off and the MGA and MGB provide the traction, with regenerative braking via the MGB [7]. The EV2 mode, where the MGA assists the MGB in providing traction, is used for smooth acceleration when the MGB cannot handle heavy loads and for starting the vehicle. Similarly, the C1 clutch is open and the C2 clutch is closed. However, the one-way clutch (OWC) is engaged every time the vehicle is started to prevent the motor from rotating as planetary gear 2 is turned by the MGA [7]. This mode is mainly used at higher loads and the average torque distribution is such that most of the vehicle's power demand is met by the MGB and the rest by the MGA, with the MGA unit also used to supplement power demand [15]. The most efficient combination of motor input torque can be selected to match output speed and torque, which increases efficiency with maximum output torque or torque distribution [31].

Low extended range mode (LERM) is a charge-sustaining (CS) mode in which the MGB and engine provide the tractive power [7]. Part of the energy provided by the engine is converted to electrical energy by the MGA to charge the battery, the engine power is distributed to the wheels via the MGA and PGS1, and the MGB provides additional torque to the wheels. This mode is activated when the C1 clutch is open, the C2 clutch is closed, and the OWC is disengaged, allowing the engine to support the power demand, and it is selected for high loads at speeds up to 60 km/h [15]. The engine torque is a function of the wheel torque required by the driver. As the C2 clutch is closed, PGS2 has a rigid speed ratio. PGS1 has a flexible speed ratio as it requires an additional engine speed control [15]. If the wheel power demand is below a certain point, the engine is allowed to generate excess power, indicating that it is being controlled within the best efficiency range rather than being used over a wide range [31].

Fixed ratio extended range mode (FERM) is a charge-sustaining mode in which the engine delivers torque to the wheels as a function of engine load and speed, and in this mode, the MGB provides a boost when required, but the MGA is locked with the clutch [7].

In this mode, both PGS1 and PGS2 are fixed to each other, and the torque is distributed between the engine and the MGB. PGS2 and PGS1 have a fixed speed relationship because clutches C2 and C1 are closed. The engine torque is a function of the transmission output speed and provides maximum power through direct mechanical contact with the wheels and additional MGB support in this mode. It operates at higher speeds from 60 km/h to over 110 km/h with higher torque demands than in the LERM mode and, as the MGA unit is not operating, both clutches are closed, and all engine power is sent to the wheels [15]. The engine cannot always operate at the optimum operating torque target line, but in this mode, the engine load is adjusted by charging or discharging the battery to stabilize the engine operating points in a highly efficient range [31].

High extended range mode (HERM) is a sustaining mode in which the ICE, MGA, and MGB operate the vehicle during peak power demand [7]. In this mode, the engine provides most of the power to the wheels and the MGB works as a generator. Both MGA and MGB are used to control the speed and load of the engine and this mode is used when the vehicle speed is greater than approximately 65 km/h with light loads or for higher torque requirements and speeds greater than 110 km/h [31]. In this mode, the engine power is split by distributing the engine power from PGS1 via the planet carrier, sun gear, and clutch C1, in which case clutch C1 is closed again and clutch C2 is opened to transmit the engine power from PGS2 [15]. PGS2 and PGS1 have a flexible speed relationship. The engine speed can be determined by an additional speed control independent of the vehicle speed [31]. The MGA works closely with the engine to control its speed and charge the battery when excess power is available [15]. As vehicle speed increases, the engine operating point is adjusted by controlling the amount of battery charge or discharge to maximize fuel efficiency [31].

2.4. Hybrid Electric Vehicle Modeling

A forward approach technique, also known as a dynamic simulation, has been used in HEV modeling to capture the time-varying behavior of the powertrain system, including the forces, torques, and accelerations involved [33–35]. It requires the development of high-precision models including dynamic transient behavior of components, which requires computational load [2,10]. The total power demand is generated by solving the vehicle's longitudinal differential equation of motion, using a PID-controlled drive model that compares the drive cycle speed with the vehicle's actual speed profile and then generates a power demand profile required to follow the vehicle's target speed profiles [10,33]. In the DDP-based optimization stages, a partially backward, i.e., quasi-static, modeling approach is used, which considers changes in the powertrain over time, and the dynamics of the system can be approximated by a set of static states [10,33,36,37]. The quasi-static map-based powertrain model calculates fuel consumption, electrical power demand and battery SOC [33]. The vehicle simulation model which consists of a controller and physical models is shown in Figure 5.

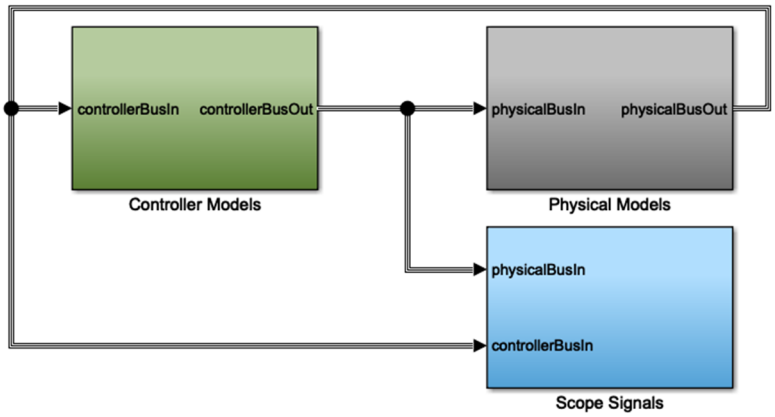

Figure 5. Hybrid electric vehicle Simulink models.

2.4.1. Internal Combustion Engine Model

The physical engine model calculates engine torque, friction, and speed, considering the inertial effects of the combustion engine and engine starting. Engine speed has different sources depending on the actual state of it and it is calculated separately for each hybrid driving mode by the physical transmission model. The engine torque is calculated according to the demand from the controller and the friction torque due to friction losses, the minimum amount of torque required by the ECU is calculated, and the minimum amount of torque required for engine operation is decided as shown in Equations (1) and (2) [38–40].

$$Tq_{ICE,Req} = p_{me} \times V_{disp} \times \frac{0.5}{2 \times pi} \quad (1)$$

$$Tq_{ICE} = \min\left(Tq_{ICE,Req} + J_{ICE} \times \dot{\omega_{ICE}}, Tq_{ICE,FL}\right) \quad (2)$$

The total pressure loss is determined with a map using the average engine nominal pressure and engine speed, also considering the engine speed, and the friction torque is calculated with Equation (3) [38–40].

$$Tq_{fric} = p_{fric} \times V_{disp} \times \frac{(0.5)}{2pi} \quad (3)$$

Considering the required engine torque and engine friction, the required indicated mean effective pressure and mean effective pressure (MEP) are calculated. Indicated mean effective pressure (IMEP) is equal to the sum of the mean effective pressure (MEP) and friction mean effective pressure (FMEP) expressed as in Equation (4) and it is also limited by a maximum pressure map as a function of the actual engine speed. Using the average peak pressure and engine parameters, engine torque is calculated by means of Equation (5). The maximum engine torque is limited by considering the full load torque [38–40].

$$p_{mi} = p_{me} + p_{mr} \quad (4)$$

$$Tq_{ICE} = p_{mi} \times V_{disp} \times \frac{(0.5)}{2pi} \quad (5)$$

where $Tq_{ICE,req}$: requested engine torque [Nm]; Tq_{ICE}: engine torque [Nm]; $Tq_{ICE,FL}$: engine torque at full load [Nm]; Tq_{fric}: engine friction torque [Nm]; J_{ICE}: engine inertia [kg·m^2]; $V_{disp:}$ engine cylinder volume [m^3]; p_{fric}: cylinder friction pressure [Pa]; ω_{ICE}: engine speed [rad/s]; $\dot{\omega_{ICE}}$: engine acceleration [rad/s^2]; p_{mi}: indicated mean effective pressure [Pa]; p_{me}: mean effective pressure [Pa]; and p_{mr}: friction mean effective pressure [Pa].

Fuel consumption is map-based and depends on engine speed, torque, and temperature [21]. The mass fuel flow rate, the total amount of fuel consumed during the simulation cycle, the specific fuel consumption, and the amount of fuel consumed during the cycle are expressed according to the following formulations [38–40].

$$FF = FC \times \frac{(\omega_{ICE} \times Tq_{ICE})}{9549} \times \frac{1}{3600} \quad (6)$$

$$FC_{Total} = \sum_{K=0}^{N} \frac{\left(\frac{(FF)}{1000}\right)}{\rho_{Fuel}} \quad (7)$$

$$FC_{Cycle} = FC_{Total} \times \frac{100}{L_{Cycle}} \quad (8)$$

where FF: fuel flow rate [g/s]; FC: specific fuel consumption [g/kWh]; ω_{ICE}: engine angular velocity [rad/s]; FC_{Total}: total fuel consumed [L]; FC_{Cycle}: specific fuel consumption in the driving cycle [L/100 km]; L_{Cycle}: total distance traveled [m]; and ρ_{Fuel}: fuel density [kg/L].

2.4.2. Electric Motor Model

The electric motor physical model calculates motor angular speed, torque, and actual electric power consumption. Using the electric motor efficiency maps, the motor efficiency is determined for each operating condition according to the operating speed and torque of the motor. Motor angular velocity and acceleration, which serves as an input for the motor moment of inertia calculation, are calculated using Equations (9) and (10) [41,42].

$$\dot{\omega_{EM}} = \frac{\omega_{EM}(k) - \omega_{EM}(k-1)}{t_i} \tag{9}$$

$$\omega_{EM} = \frac{2 \times pi \times n}{60} \tag{10}$$

where ω_{EM}: electric motor actual angular speed [rad/s]; $\dot{\omega_{EM}}$: electric motor acceleration [rad/s^2]; t_i: sampling time [sec]; and n: motor speed [rpm].

The motor mechanical power is calculated as a function of the actual motor torque and speed using Equation (11) which is limited according to the maximum power [42,43].

$$P_{EM,Mech} = Tq_{EM,\ act} \times \omega_{EM} \tag{11}$$

Motor power losses are determined map-based as a function of speed and torque. Electrical motor power is the sum of the mechanical power and losses plus inertia effects. Mechanical motor power is calculated using Equation (11), the electrical power using Equation (12), and the current using Equation (22) [42,43].

$$P_{EM,Elec} = P_{EM,Mech} \pm J_{EM} \times \dot{\omega_{EM}} \times \omega_{EM} + P_{EM,\ Loss} \tag{12}$$

The current drawn from the motor is the ratio of the electrical power to the actual battery voltage and is calculated using Equation (13) [42,43].

$$I_{Elec} = \frac{P_{EM,Elec}}{V_{Batt,Act}} \tag{13}$$

where $P_{EM,Mech}$: motor mechanical power [W]; $P_{EM,Elec}$: motor electrical power [W]; $P_{EM,Max}$: motor maximum power [W]; $P_{EM,Loss}$: motor loss power [W]; $Tq_{EM,act}$: motor actual torque [Nm]; J_{EM}: motor inertia [kg·m^2]; $V_{Batt,Act}$: battery actual voltage [V]; and I_{Elec}: motor current [A].

2.4.3. Transmission Model

Depending on the hybrid driving modes, the engine speed required for gear shifting is calculated as a function of vehicle speed (equal to the maximum idle speed) in the HERM mode and depending on the gear ratio in the LERM and FERM modes, and it is gradually transmitted to the front differential using a specific gradient limiter. The mechanical transmission models include different vehicle operating modes and calculate the torque at the wheel level considering the gear ratios of the MGA, MGB, and engine. It also evaluates transmission losses, considering the mechanical efficiency of the gearbox and differential. The transmission power transmission efficiency is determined based on the map-based operating speed and torque, and the losses are calculated as follows [21,44].

$$P_{trsm,loss} = P_{trsm,out} - P_{trsm,in} \tag{14}$$

The relationship between transmission input and output speed depends on the gear ratio and is calculated using Equation (15) and transmission input torque is calculated using Equation (16) [21,44].

$$\omega_{trsm,in} = r_{gear} \times \omega_{trsm,out} \tag{15}$$

$$Tq_{trsm,in} = \frac{1}{r_{gear}\varepsilon_{trsm}} \times Tq_{trsm,out} + J_{trsm}(in,\ out) \tag{16}$$

where $P_{trsm,loss}$: transmission power losses [W]; $P_{trsm,out}$: transmission output power [W]; $P_{trsm,in}$: transmission input power [W]; $\omega_{trsm,in}$: transmission input speed [rad/s]; $\omega_{trsm,out}$: transmission output speed [rad/s]; r_{gear}: transmission gear ratio [-]; J_{trsm}: transmission inertia [kg·m^2]; $Tq_{trsm,in}$: transmission input torque [Nm]; $Tq_{trsm,out}$: transmission output torque [Nm]; and ε_{trsm}: transmission efficiency ratio [-].

The planet–sun gear ratio calculations are modeled as in Figure 6 and the planetary gear ratio, gear speeds, and torque power are calculated as follows [21,36,44].

$$P_{C1} = P_{R1} + P_{S1} \tag{17}$$

$$N_{C1} = \frac{1}{r_{PGS1}+1}N_{S1} + \frac{r_{gear}}{r_{PGS1}+1}N_{R1}\ and\ (r_{PGS1} = \frac{Z_{R1}}{Z_{S1}}) \tag{18}$$

$$T_{S1} = \frac{1}{r_{PGS1}+1}T_{C1} \quad and \quad T_{R1} = \frac{r_{PGS1}}{r_{PGS1}+1}T_{C1} \tag{19}$$

$$N_{S1} = N_{R2} \quad and \quad N_{C1} = N_{C2}\ (\text{in HERM mode}) \tag{20}$$

where P_{C1}: carrier gear power [W]; P_{R1}: ring gear power [W]; P_{S1}: sun gear power [W]; N_{S1}: sun gear speed [rpm]; N_{R1}: ring gear speed [rpm]; N_{R2}: second ring gear speed [rpm]; N_{C1}: carrier gear speed [rpm]; N_{C2}: 2nd carrier gear speed [rpm]; Z_{R1}: ring gear distance [m]; Z_{S1}: sun gear distance [m]; T_{C1}: carrier gear torque [Nm]; T_{S1}: sun gear torque [Nm]; T_{R1}: ring gear torque [Nm]; and r_{PGS1}: PGS1 ratio [-].

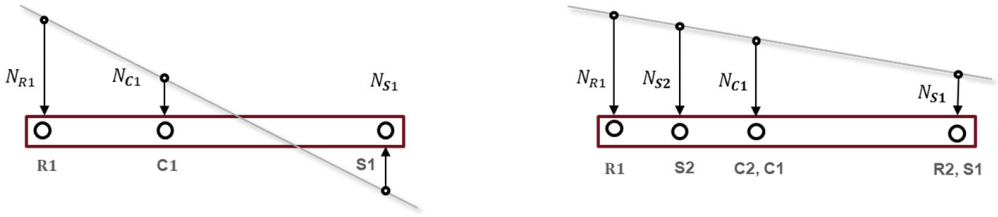

Figure 6. Planetary gear ratio model.

Torque input to the final drive is calculated using Equation (21), considering the transmission models MGA, MGB, and ICE. Torque at the front axle is calculated using Equation (22) [21,44].

$$\begin{aligned} Tq_{Fr\_diff\_in} = {} & Tq_{ICE} \times \tfrac{1+r_{PGS1}}{r_{PGS1}} \times r_{eff\_PGS1} \\ & + Tq_{EM,act} \times (1 + r_{PGS2}) \times r_{eff\_PGS2} \end{aligned} \tag{21}$$

$$Tq_{Fr\_Whl} = Tq_{Fr\_diff\_in} \times r_{eff\_Fr\_diff} \times r_{Fr\_diff\_in} \tag{22}$$

where $Tq_{Fr\_diff\_in}$: front differential input torque [Nm]; Tq_{ICE}: engine torque [Nm]; $Tq_{EM,act}$: motor actual torque [Nm]; Tq_{Fr_Whl}:: front wheel torque [Nm]; r_{PGS1}: PGS1 ratio [-]; r_{PGS2}: PGS2 ratio [-]; $r_{\mathrm{Fr}\_diff\_in}$: front differential ratio [-]; $r_{eff_{PGS1}}$: PGS1 efficiency [-]; r_{eff_PGS2}: PGS2 efficiency [-]; and $r_{eff\_Fr\_diff}$: front differential efficiency [-].

2.4.4. Battery Model

The battery control model determines the limits of the current and electrical power depending on the *SoC* and battery voltage and calculates the maximum electrical battery power for peak and continuous modes depending on the battery *SoC* and temperature. The internal open-circuit resistance in the battery pack is map-based [43]. Total open circuit voltage and internal resistance of the battery are determined using Equations (23) and (24) [45,46].

$$V_{Batt,OC} = N_{Cell,series} \times V_{Cell,OC} \tag{23}$$

$$R_{Int} = R_{Cell} \times \frac{N_{Cell,series}}{N_{Cell,paralel}} \quad (24)$$

where $V_{Batt,OC}$: battery open circuit voltage [V]; $V_{Cell,OC}$: cell open circuit voltage [V]; R_{Int}: battery internal resistance [ohm]; R_{Cell}: cell internal resistance [ohm]; $N_{Cell,series}$: serial cells [-]; and $N_{Cell,paralel}$: parallel cells [-].

The battery current can be calculated from Equation (25), the actual battery voltage from Equation (26), and the battery power from Equation (27) using a simple circuit model with open circuit voltage and internal resistance as shown in Figure 7 [33,43,46].

$$I_{Batt,Act} = \frac{\left(V_{Batt,OC} - \left(V_{Batt,OC}^2 - 4P_{Batt,Req} \times R_{Int}\right)^{\frac{1}{2}}\right)}{2R_{int}} \quad (25)$$

$$V_{Batt} = V_{Batt,OC} - R_{Int} \times I_{Batt} \quad (26)$$

$$P_{Batt,\ Act} = V_{Batt,Act} \times I_{Batt,Act} \quad (27)$$

where $P_{Batt,Req:}$ requested battery power [W]; $I_{Batt,Act}$: battery current [A]; and $V_{Batt,Act}$: battery voltage.

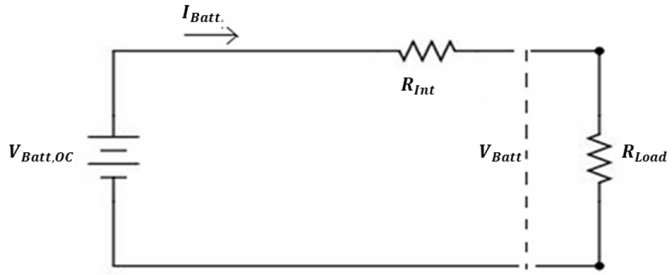

Figure 7. Battery open loop voltage and cell internal resistance [43].

The state of charge (*SoC*) of the battery is calculated using Equation (28). The initial capacity of the battery is calculated using Equation (30). For the capacity variation, the positive (discharge) and negative (charge) current are multiplied by the coulombic efficiency as shown in Equation (29) and integrated [21,43,46].

$$SoC = \frac{(Q_{ini} - \Delta Q)}{Q_{ini}} = \frac{\left(Q_{CapCell} \times N_{Cell,Parallel} \times SoC_{ini} - \frac{\int i_{BattAct} \cdot dt}{3600}\right)}{Q_{CapCell} \times N_{Cell,Parallel}} \quad (28)$$

$$\Delta Q = \int i_{BattAct} \times dt \times \eta C \quad (29)$$

$$Q_{ini} = Q_{CapCell} \times N_{Cell,Parallel} \times SoC_{ini} \quad (30)$$

where *SoC*: battery charge status [%]; Q_{ini}: initial state of charge [Ah]; ΔQ: capacity change [Ah]; $Q_{CapCell}$: cell capacity [Ah]; SoC_{ini}: initial state of charge [%]; $i_{BattAct}$: battery actual current [A]; and ηC: columbic efficiency [-].

2.4.5. Vehicle Model

In the physical vehicle model, wheel traction torque is calculated using Equation (31) via vehicle resistance such as air resistance, gravity resistance, rolling resistance, and inertia resistance as shown Figure 8 [47,48].

$$Tq_{Whl} = (F_{Air} + F_{Acc} + F_{Grd} + F_{Roll}) \times r_{Whl} \quad (31)$$

where Tq_{Whl}: wheel torque [Nm]; F_{Air}: air resistance force [Nm]; F_{Acc}: acceleration resistance force [Nm]; F_{Grd}: slope resistance force [Nm]; F_{Roll}: rolling resistance force [Nm]; and r_{Whl}: dynamic wheel radius [m].

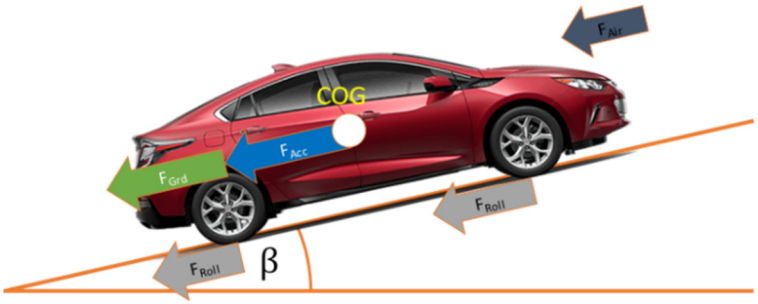

Figure 8. Forces acting on the vehicle [21].

The air resistance force acting on the vehicle is calculated depending on the vehicle speed using Equation (32), the resistance force due to a sloping road using Equation (33), the rolling resistance forces using Equation (34), and the acceleration resistance force reduced to the wheel level using Equation (35) [48,49].

$$F_{Air} = \frac{1}{2} \times \rho_{Air} \times A_{Drg} \times c_{Drg} \times v_{Veh\_act}^2 \tag{32}$$

$$F_{Grd} = m_{Veh} \times g \times \sin(\beta) \tag{33}$$

$$F_{Roll} = m_{Veh} \times g \times sign(v_{Veh\_act}) \times \left(f_{r0} + f_{r1} \times |v_{veh\_act}| + f_{r2} \times v_{Veh\_act}^2\right) \tag{34}$$

$$F_{Acc} = \left(\frac{2J_{Whl}}{r_{Whl}^2} + m_{Veh}\right) \times a_{Veh\_act} \times f_{Veh\_F\_Acc} \tag{35}$$

where ρ_{Air}: air density; A_{Drg}: front drag area [m^2]; c_{Drg}: drag coefficient; v_{Veh_act}: actual vehicle speed [m/s]; β: angle of climb [rad]; $a_{Veh_{act}}$: actual vehicle acceleration [1/s^2]; m_{Veh}: vehicle mass [kg]; J_{Whl}: wheel inertia; r_{Whl}: dynamic wheel radius [m]; $f_{Veh\_F\_Acc}$: acceleration factor [-]; f_{r0}: zero-order deceleration value [-]; f_{r1}: first-order deceleration value [-]; and f_{r2}: second-order deceleration value [-].

The normal wheel force due to braking is limited to the maximum wheel torque compared to the actual transmission torque and calculated using Equation (36) [48,49].

$$Tq_{Whl\_max} = F_{Whl} \times r_{Whl} \times r_{Mu\_Veh} \tag{36}$$

where Tq_{Whl_max}: maximum axle torque [Nm]; F_{Whl}: wheel traction force [N]; and r_{Mu_Veh}: coefficient of road grip [-].

2.4.6. Driver Model

In the driver model, vehicle torque demand at the wheel and the braking torque demand are calculated from the output of the driving cycles and the actual vehicle speed using a speed-based PI controller, considering the vehicle/drivetrain inertia and vehicle driving resistance such as air resistance, rolling resistance, and gradient resistance. Then, this value is added to the output of a PI controller with the following equation and the speed difference is defined by the following equation [50].

$$Tq_{PI,req} = K_p \times (\Delta v) + K_i \times \int (\Delta V) \times dt \quad where \quad \Delta v = v_{Veh\_req} - v_{Veh\_act} \tag{37}$$

The wheel torque demand is calculated using the following equation. The pre-torque demand is expressed in the previous section by Equation (38) [50].

$$Tq_{Whl,req} = Tq_{Pre,req} + Tq_{PI,req} \tag{38}$$

where $Tq_{Whl,req}$: wheel torque requested [Nm]; $Tq_{Pre,req}$: pre-torque demand [Nm]; $T_{PI,req}$: controller wheel torque request [Nm]; v_{Veh_req}: requested vehicle speed [m/s]; v_{Veh_act}: ac-

tual vehicle speed [m/s]; Δv: vehicle speed difference [m/s]; K_p: controller proportional coefficient [-]; and K_i: controller integral coefficient [-].

2.5. Drive Cycles

Different driving cycles can be simulated using predefined map-based speed and slope profiles shown in Figure 9. UDDS is a standard driving cycle used in the EU to analyze fuel consumption and emissions in urban driving conditions and reflects typical urban driving conditions such as stop-and-go traffic, low speeds, and frequent turns [6,51–54]. The JC08 driving cycle is a standardized test procedure used in Japan to evaluate the fuel consumption and exhaust emissions of gasoline passenger cars under urban driving conditions, which was developed to better suit Japanese driving conditions [55,56]. FTP75 cycle is a standardized test procedure in the US to evaluate the performance, fuel consumption, and emissions of light-duty vehicles in typical urban conditions such as stop–start traffic and low-speed driving [53,57]. HWFET driving cycle is a standardized test procedure used by the US Environmental Protection Agency (EPA) to evaluate the fuel consumption and emissions of vehicles by representing real-world highway driving conditions in a driving scenario which involves higher speeds and longer durations compared to the city driving cycles [6,53,58]. NEDC is a standardized test procedure developed by the EU in the 1970s to assess the efficiency, performance, fuel consumption, and emissions of vehicles in urban and non-urban driving conditions [53,59,60]. The urban cycle represents driving conditions in urban areas with frequent stops and starts, lower speeds, and shorter distances. The non-urban cycle represents driving conditions on open roads with higher speeds and longer distances [6,59,60]. Although NEDC has been widely used for vehicle certification and regulatory purposes, it has been criticized for not accurately representing real-world driving conditions and under-estimating fuel consumption and emissions [61,62]. WLTC is a standard test cycle developed to provide a more realistic representation of road driving conditions than NEDC. WLTC is a test protocol that simulates more realistic driving conditions and covers a longer cycle and has been adopted as the new type of approval test cycle for the certification of fuel consumption and emissions of passenger cars and light commercial vehicles in Europe from 2017 [61–63].

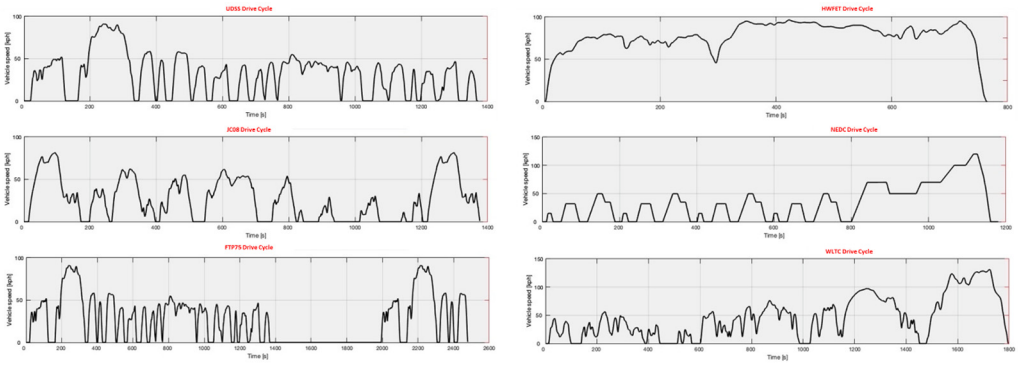

Figure 9. Drive cycles used for simulations.

3. Hybrid Electric Vehicle Model Validation

To validate the high accuracy of the simulation results, the vehicle was activated to operate in the charge-sustaining mode (CS) depending on the battery initial charge (*SoC*) value according to the measurements taken from the vehicle chassis dynamometer for the UDDS driving cycle and the model simulation results were compared with the actual test data. Evaluation of the simulation model maturity performed against measurement data and resulting plots show that the simulation model is capable of reflecting the vehicle behavior in an appropriate accuracy level according to the defined evaluation criteria.

In the vehicle simulation model, the mechanical energy consumption during the propulsion phase and braking phase based on torque and power in the wheels at a given vehicle velocity and driving distance shows up to a 3.4% deviation. In the transmission

model, mechanical energy and power during the propulsion phase and braking phase based on torque and power in the wheels at a given transmission input shaft speed and torque showed up to a 2.5% deviation, which can be accepted as a good deviation level. In the electric motor model, mechanical and electric power and energy during the propulsion phase and braking phase based on average speed and torque showed up to a 3.7% deviation. In the HV battery model, battery *SoC* showed around a 1% deviation, and energy charging and discharging based on electrical power and energy based on average voltage and current showed up to a 4% deviation. In the internal combustion engine model, cumulative fuel consumption based on average speed and torque shows around a 3.5% deviation which could be considered as a good deviation level. As can be seen from the simulation results in Figures 10 and 11, the model and the applied rule-based driving strategy can reflect the vehicle behavior with good accuracy.

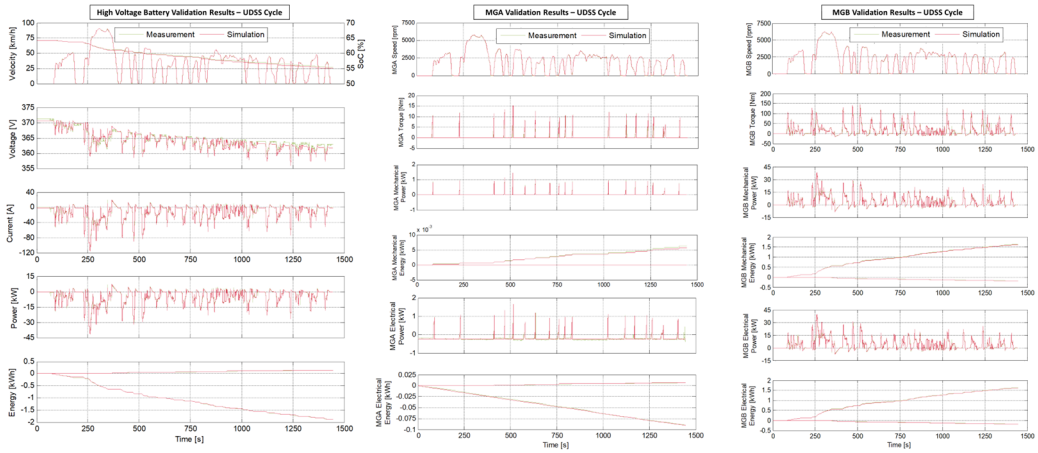

Figure 10. Battery and MGA and MGB validation results for UDDS-CS.

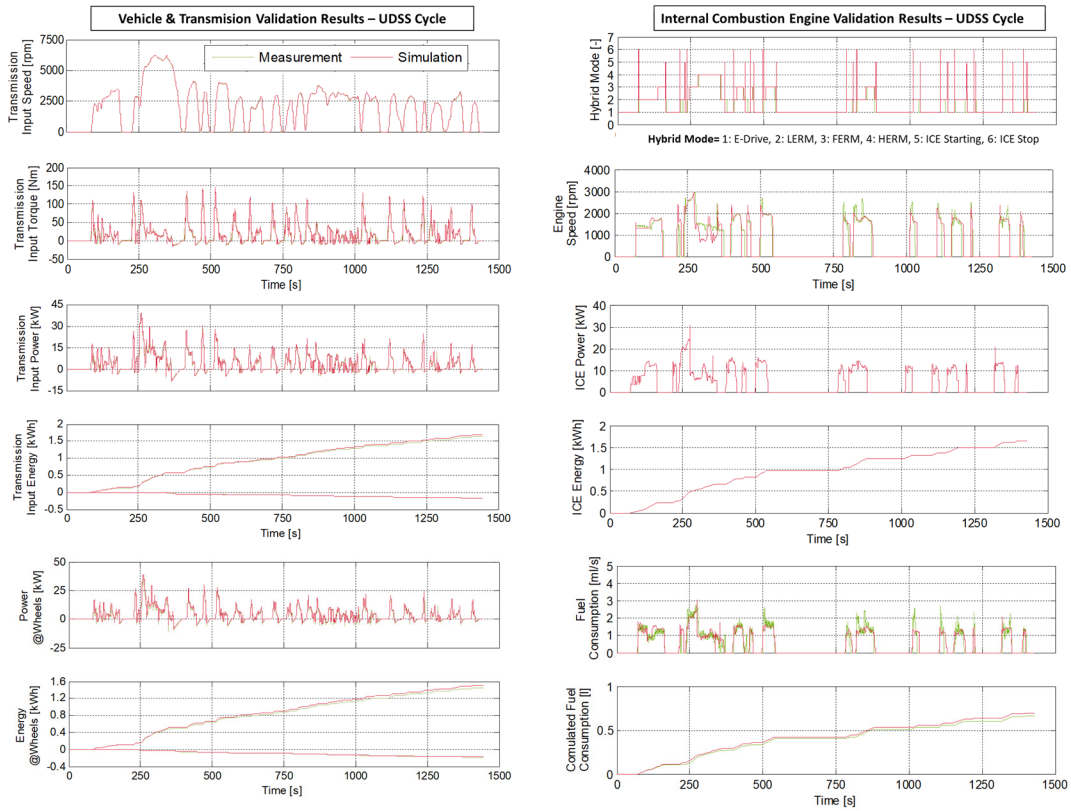

Figure 11. Vehicle and transmission and ICE validation results for UDDS cycle.

4. Hybrid Electric Vehicle Energy Management Systems

4.1. Energy Management Systems Objectives

Energy management strategies aim to increase efficiency and performance by optimizing the power distribution between the engine and the electric motor in HEVs, considering complex driving conditions, aim to maximize fuel economy and performance, and also aim to reduce emissions [2,5,6,10,53,56,64–68]. By improving powertrain efficiency through advanced optimization techniques in HEV EMS, researchers aim to further improve fuel economy and emission reduction [1,10,20,33,69,70].

EMS aims to improve the drivability and overall user experience of HEVs, ensuring smooth power delivery and responsive performance [29,64,66,67,71]. It can adapt to different driving conditions and traffic patterns by optimizing the operation of the powertrain for maximum efficiency and performance [6,11,58]. It can incorporate real-time traffic information to optimize power distribution and improve energy efficiency according to driving conditions [52,72,73]. It considers various constraints such as power demand, *SoC*, and system limitations to ensure the safe and reliable operation of HEVs [6,53,64,68,74]. EMSs can optimize electric motor and battery utilization, allowing for longer electric driving range in HEVs [10,58,75,76]. EMSs maximize the capacity and extend the lifetime of the battery by enabling its efficient use in HEVs [12,29,67,74,77–79]. It includes strategies to protect the battery and other components, which helps to extend battery life and reduce maintenance costs [6,73,77].

4.2. Classification of Energy Management Systems

Energy management systems are basically divided into two parts, which are online and offline strategies. Online strategies involve real-time control and decision making based on current driving conditions and vehicle states. These strategies adaptively adjust the power distribution between the engine and the electric motor to optimize performance and efficiency [6,34,80–83]. Online control strategies are based on local optimization and can be implemented in real-time since no driving cycle prior knowledge is required and there is a limited computational load [2,6,10,20]. Offline energy management strategies are designed before real-time implementation using historical driving data or simulation models and provide optimized power management solutions [53,68,71,82,83]. Offline optimization requires a priori knowledge about upcoming driving cycles and searches for a global optimal solution [2]. Although they cannot be directly used in real vehicles due to the computational complexity, they serve as a benchmark to calibrate the control parameters of other EMSs, which can be effectively used to reduce fuel consumption [2,20]. Offline EMSs are divided into rule-based and optimization (local and global)-based EMSs, and each approach has different advantages in terms of computational load and optimality [20]. Optimization-based strategies can result in lower fuel consumption compared to rule-based strategies [1,84].

The optimal discharge strategy of the battery, which consists of operating the vehicle as an electric vehicle until the battery is depleted and then continuing the charge maintenance process as a conventional HEV using the engine, is referred to as the charge-depletion/charge-sustaining (CD/CS) strategy [4,32,36]. The use of the stored electrical energy is guaranteed, and no knowledge of the future driving task is required, which is the main advantage of this strategy [84]. If the desired output trajectory is known in advance when the vehicle follows a given driving cycle, dynamic programming and analytical optimal control techniques can then be used to obtain the theoretical optimal results [5]. Unlike CD-CS, which can be applied without any knowledge of the future trip, a global optimal strategy such as PMP guarantees optimality only if the speed and altitude profiles are known in advance [4]. The PMP algorithm aims to obtain a blended trajectory of the *SoC* to minimize the fuel consumed, which results in an overall better performance than the CD-CS strategy [32]. The main objective of the optimization-based power management method is to find the optimal control results to minimize the process cost over a given horizon [2,5]. Power splitting represents a typical optimal control problem since it usu-

ally depends on the real objective of minimization of a given cost function, such as fuel consumption [10].

4.3. Rule-Based Energy Management System

HCU controls the driving mode of the vehicle, including torque distribution between different power sources such as the engine and electric motors, regenerative braking, and engine speed control in specific hybrid operation, acting as a master controller for all slave controllers such as the engine, battery, motors, and transmission controllers. Rule-based strategies, based on a set of rules that aim to selectively maintain the power distribution among the energy sources with high efficiency by observing the operating conditions of the vehicle, are widely used due to their reliability and satisfactory fuel consumption results [10,32,57,85,86]. Although they often produce results that are far from optimal despite their low computational requirements, they are easy to implement in real-time applications because they consist of empirical rules and thresholds defined by analyzing the performance and characteristic maps of the components used in the system [6,10,36,65,80,87,88].

This method depends mainly on logical rules and local constraints rather than having prior knowledge of the driving cycle, and that is why it is less adaptive to changing driving conditions [2,20]. The rule-based controller depends on both powertrain components and vehicle architecture [33,36]. It requires a large amount of time and engineering to develop the strategy due to the lengthy rule definition and calibration process and is highly dependent on driving conditions [6,86,89].

As shown in Figure 12, the hybrid driving mode control model, in which all possible vehicle states are defined, uses state transition diagrams to determine the mode of operation among five possible modes, namely single/dual motor electric driving (ED1–ED2), engine start, engine stop, regenerative braking, low extended range (LERM), high extended range (HERM), and fixed extended range (FERM). It also implements engine speed control and *SoC*-based control. The main parameters influencing mode selection are driver torque demand, vehicle speed, and battery *SoC*. Calibration thresholds are calibrated for each of the five different operating modes [21].

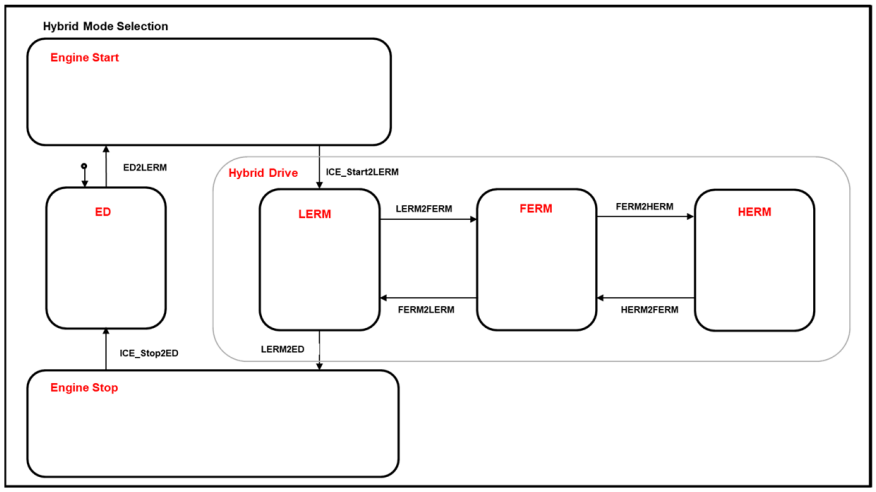

Figure 12. Hybrid mode selection diagram of HCU.

The control rules defined in hybrid mode selection are converted by the HCU signals into function calls, where the torque distribution and engine speed are defined according to the defined rules. HCU controls the torque distribution between the components by calculating the speed of PGS1 and PGS2 according to the wheel torque, vehicle speed, and operating modes requested by the driver. It also considers the physical operating limits of all components in the system. For example, the torque demand of the hybrid controller for the MGA is compared with the maximum engine torque, or the electrical power demand

is also considered to ensure that it can provide the current that can be drawn from the battery pack [43]. Operating mode separation is controlled by user command, considering the effects of electric drive, hybrid operation, vehicle speed, wheel torque demanded by the driver, engine speed, ambient temperature, battery *SoC*, previous operating mode, etc., in addition to hybrid operation. In this way, successive transitions between electric driving (EV1-2) and hybrid driving (LERM, FERM, and HERM) are made within a certain hysteresis range defined in the maps and according to the vehicle operating conditions, as shown in Figure 12.

In the rule-based controller, a set of logical rules is predefined using the component efficiency maps to determine the optimal power distribution between the engine and the electric motor, considering the simultaneous efficiency of the engine and the electric motor and the SOC of the battery [20,86]. Depending on the battery SOC and vehicle load, the engine is used at higher loads where its efficiency is better, while the electric modes should be preferred at lower loads [20,36]. In *SoC*-based control, the engine load is applied as a function of the *SoC*: in LERM mode due to the low-medium load demand of the engine and in FERM mode due to the medium load demand of the engine. In HERM mode, it is not applied due to the high load demand of the engine and the low efficiency of the MGB. As the engine provides an extra degree of freedom in LERM and HERM modes and is frequently engaged, engine speed control is particularly important for the functions performed by the MGA. Power-split control can be performed to meet the driver's power demand and keep the *SoC* within a certain range [20]. If the *SoC* of the battery pack is below the critical threshold, as shown in Figure 13, the electric motors are switched off and the engine is activated [15,21,43].

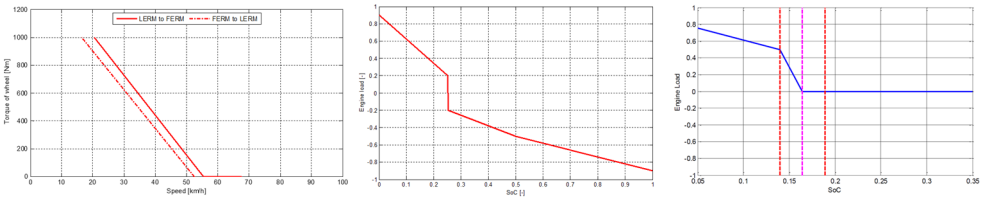

Figure 13. Mode transition maps; engine load variation based on *SoC*.

4.4. Discrete Dynamic Programming (DDP)-Based Energy Management System

DDP is based on the optimality principle of Richard Bellman in the 1950s and aims to find optimal control policies using a multi-stage decision process, with the property that an optimal control policy is one in which, whatever the previous decision, the remaining decisions should form the optimal policy with respect to the situations arising from the previous decisions [2,6]. DDP is based on the concept of decomposing a nonlinear dynamic optimization problem into discrete time sub-problems, where a cost function is generated at each step time [2,68,83].

DDP suffers from the significant computational time required to solve the backward time optimal problem from the future state to find the first control input in a feasible range, and the computational burden increases as the size of the system increases [2,6,20,43]. Due to the high computational load and the need to have prior knowledge of the driving cycle, a real-time controller must operate with limited computational and memory resources, so it cannot be directly applied to real-time control because it is impossible to know the future driving conditions such as speed, road gradient, and traffic dynamics [1,5,20,33,90].

DDP is known to search for the global optimal solution when there is complete information about the driving cycle, and the need for a backward-looking procedure means that the solution can only be obtained offline for a previously known driving cycle [2,10,20,33]. DDP evaluates the minimum fuel economy that can be achieved during a driving task to reach the global optimum by analyzing the entire driving cycle [1,33]. The global optimum strategy based on DDP involves a combination of fuel and electrical energy consumption throughout the driving cycle, and the distance of the driving cycle must be known to use all the energy in the battery for the global optimum strategy [84].

The model equation may contain various state and input variables, and the equations may contain time-varying state and input constraints. It should specify the number of controllers to be optimized, the system states to be monitored, and the limits for each [33]. The dynamic programming technique guarantees global optimality by solving comprehensively for all control and state variables [5]. The most efficient combinations of power distributions between components can be calculated using dynamic programming [33,43].

The DDP-based multi-stage optimization problem consists of two stages to find the most optimal control parameters. In the first stage, backward optimization of the control domain is performed, and then forward simulation is performed to select the appropriate control variable. In backward optimization, the optimal set of control variables is obtained by proceeding backwards from the final state and selecting the path that minimizes the operating cost each time. When solving a problem using the backward dynamic programming technique, the obtained co-products are the optimal values of each state from each stage to the end, whereas when solving a problem using the forward dynamic programming, the corresponding co-products are the optimal values from the initial states in the first stage to each state in the remaining stages [6].

Dynamic programming is a multi-stage decision process that applies the optimal principle to make hierarchical decisions and solve optimal controls [84]. For an optimal decision, whatever the initial state and decision (stage cost) $L(u_k, x_k)$, the remaining decisions (ongoing cost) $J^*_{k+1}(x_{k+1})$ must be optimal for the initial decision; that is, the second part of the optimal trajectory is also the optimal trajectory. The equation for the multi-stage decision process is expressed using Equations (39) and (40) [84].

$$J^*_k(x_k) = min_{u_k}\{L(u_k, x_k) + J^*_{k+1}(x_{k+1})\} \tag{39}$$

$$u^*_k = argmin_{u_k}\{L(u_k, x_k) + J^*_{k+1}(x_{k+1})\} \tag{40}$$

$J^*_k(x_k)$ in the above equation is the optimal value function of the k-stage decision process from the initial state to the final state. The parameter u_k in the formation is the control strategy of the k-stage decision process in the initial state x_k; therefore, the state is transferred to the next state [84]. By discretizing the parameters x_k and u_k in the equation to the finite states, the above equation is solved backwards, the optimal control and the corresponding cost are stored, and then the optimal solution with specific initial states is carried forward by applying optimal controls along the horizon [5].

The optimal control problem is to minimize the fuel consumption during vehicle operation cycle while respecting the design constraints of each component and the drivability/performance specifications. The objective is to minimize a cost function (integral cost) defined as an integral over a finite horizon (driving cycle) [33]. The cost function to be minimized usually consists of fuel economy and other performance parameters, where the total fuel consumption is minimized as follows [5]. The optimal control problem is defined as below.

$$\min J = \int_{to}^{tf} \dot{m}_f \times dt \tag{41}$$

Control and state variables are defined as below.

$$u = [u_1, u_2, u_3]^T \tag{42}$$

$$x = [x_1, x_2\,]^T \tag{43}$$

where u_1: Tq_{ICE} (engine torque); u_2: N_{ICE} (engine speed); u_3: Tq_{MGB} (MGB torque); x_1: SoC; and x_2: I_mode.

By discretizing the problem and selecting the combination with the minimum fuel cost, the minimum cost of each mode is calculated offline, and the obtained control is stored as a table for the given combination [84]. The optimal control problem is defined as follows

by specifying the equality and physical limits and constraints in the equation. The power balance equality bounds are expressed by the following formula.

$$P_{Whl} = P_{ICE} + P_{MGA} + P_{MGB} \tag{44}$$

where P_{Whl}: wheel power [W]; P_{ICE}: engine power [W]; P_{MGA}: MGA power [W]; and P_{MGB}: MGB power [W].

The physical limits at each step must be respected, the *SoC* must be kept within a certain range to reduce battery degradation, and at each instant, the total torque output of the powertrain must be equal to the demand of the drive. At each instant, it cannot exceed the maximum torque/power ratio of the powertrain components; similarly, the total battery power must remain within acceptable limits in both charging and discharging modes [33]. Electric machines and the engine should be limited to certain speeds to ensure the operational reliability of the system [5]. The maximum motor power limitation is achieved by keeping the operating torque and speed of the motor within specified ranges. Limits and constraints in the equation are specified as below.

$$Tq_{ICE,max} \geq Tq_{ICE} \geq Tq_{ICE,min} \tag{45}$$

$$N_{ICE,max} \geq N_{ICE} \geq 0 \tag{46}$$

$$Tq_{MGA,max} \geq Tq_{MGA} \geq Tq_{MGA,min} \tag{47}$$

$$N_{MGA,max} \geq N_{MGA,min} \tag{48}$$

$$Tq_{MGB,max} \geq Tq_{MGB} \geq Tq_{MGB,min} \tag{49}$$

$$N_{MGB,max} \geq N_{MGB,min} \tag{50}$$

$$P_{Batt,max} \geq P_{bat} \geq P_{Bat,min} \tag{51}$$

where Tq_{ICE}: engine torque [Nm]; Tq_{MGA}: MGA torque [Nm]; Tq_{MGB}: MGB torque [Nm]; P_{Batt}: wheel power [W]; N_{ICE}: engine speed [rpm]; N_{MGA}: MGA speed [rpm]; and N_{MGB}: MGB speed [rpm].

From the operating limits of the system, the battery *SoC* limits are constrained within the minimum allowable value SoC_{min} and the maximum allowable value SoC_{max}. In addition, the penalties due to mode changes are expressed as follows.

$$SoC_{max} \geq SoC \geq SoC_{min} \tag{52}$$

$$Mod_{max} \geq Mod \geq Mod_{min} \tag{53}$$

4.5. Pontryagin's Minimum Principle (PMP) based Energy Management System

Pontryagin's Minimum Principle was developed by the Russian mathematician Lev Pontryagin in 1956 to solve the global optimization problem and is a special case of the Euler–Lagrange equation for the computation of variations [2,6]. This principle states that the optimal solution to the global optimization problem must satisfy the optimality condition and is based on the instantaneous minimization of the Hamiltonian function over a driving cycle [6,32,91,92]. The optimal trajectory obtained from PMP is the unique trajectory that satisfies the necessary and boundary conditions [5,6].

PMP is not suitable for real-time applications because the initial cost depends on the driving cycle, and different driving cycles require different optimal initial cost values, as the size of the look-up table grows exponentially and increases the computational loads [2]. PMP does not guarantee optimality unless information about the future driving state is provided [20]. The optimization problem aims to minimize the fuel consumed by the vehicle in each drive cycle, while meeting the torque required by the driver and satisfying the physical constraints of the powertrain components [32].

The main principle of the PMP algorithm is to search for the optimal control variable u(t) such that the Hamiltonian function takes the minimum value [85]. This cost, also known as the performance criterion, J, is the total fuel consumed during a driving cycle. The hybrid controller should minimize the fuel consumed by the engine during the trip, subject to static and dynamic constraints of various vehicle components [93]. The energy management problem is inherently a constrained optimization problem where the objective function (J) is minimized under system dynamic constraints, local constraints on state and control, and finally global constraints on the system as below [32,94].

$$J = \int_{to}^{tf} \dot{m_f}(u(t),\ t) \times dt \tag{54}$$

where $u(t)$ is the control action; $\dot{m_f}$: instantaneous fuel consumption rate; and $[\,t_0, t_f\,]$ is the optimization horizon [32]. Control and state variables are defined as follows.

$$u = [u_1, u_2\,]^T \tag{55}$$

$$x = [x_1, x_2\,]^T \tag{56}$$

where u_1: Tq_{mgb}: MGB torque; u_2: N_{eng}: engine speed; x_1: SoC; and x_2: I_{mod} (mode of operation).

By following an optimal trajectory of the SOC from a given initial value to a final value without violating the global constraints of the SOC and the physical limitations of the engine, the electric machines, and the battery pack, the minimum fuel consumption during the drive can be achieved [93]. Hamiltonian function is calculated as follows and the optimal solution is found numerically.

$$\mathrm{H}\ (\mathrm{x},\ \mathrm{u},\ \lambda,\ \mathrm{t}) = P_f(u,t) + \lambda \times P_{be}(x,u,t) = \dot{m_f}(u(t),t) + \lambda \times f(x(t),u(t),t) \tag{57}$$

where P_f: fuel combustion power [W]; λ: the equivalence factor; and $P_{be:}$ the electrochemical battery power [W]. λ: common state variable.

PMP allows the global optimization problem to be reduced to a local instantaneous problem that involves finding the optimal control sequence $u(t)$ that minimizes the Hamiltonian function at each instant of time [32]. The necessary optimality conditions are expressed using Equations (58) and (59).

$$\dot{x^*}(u(t),t) = \frac{\partial H}{\partial \lambda} = f(x(t),u(t),t) \tag{58}$$

$$\dot{\lambda^*}(t) = -\frac{\partial H}{\partial \lambda} = -\lambda(t) \times \frac{\partial f(x(t),u(t),t)}{\partial x} \tag{59}$$

PMP conditions transform the general optimization problem into a local problem. The Hamiltonian function is minimized exactly at $u(t) = u(t)$*. The optimal control problem is defined using Equation (60).

$$u_k^* = argmin_{u_k}\{H(x,u,\lambda,t\ )\} \tag{60}$$

PMP states that if the control law $u^*(t)$ is optimal for the following equation, then the following conditions must be satisfied as a necessary but not sufficient condition [5]. Restricted boundary values must be respected when minimizing the Hamiltonian function, i.e., for the upper boundary and lower boundary.

$$x^*(t_0) = SoC_{initial} = SoC_0 \tag{61}$$

$$x^*\left(t_f\right) = SoC_{min} = SoC_f \tag{62}$$

By using the condition $u^*(t)$ = argmin(H) to identify a candidate solution, the equilibrium can be solved numerically using an iterative method, since a boundary condition is defined at the end point, and this iterative method consists of replacing the two-point boundary value problem by a conventional initial condition problem [5].

The necessary condition according to PMP constrains the optimal control trajectory ($u^*(t)$), the optimal state trajectory ($x^*(t)$), and the optimal co-state trajectory ($\lambda^*(t)$) to minimize the Hamiltonian function as follows:

$$\mathrm{H}\left(x^*(t),\ u^*(t), \lambda^*(t),\ t\right) \leq \mathrm{H}\left(x^*(t),\ u(t), \lambda^*(t), t\right) \tag{63}$$

The torque and speed of the transmission gears are calculated as described in Section 2. The power is determined by Equation (57). The integral constraints are related to the initial and final values of *SoC*, SoC_{t0}, and SoC_{tf} during the operation of the vehicle over a given driving profile [32]. Similarly, there are constraints on the state and control variables that must be satisfied at each instant. Physical constraints are also applied at each instant to ensure that the total power demand at the wheels is met while minimizing the Hamiltonian parameter [32]. At any given moment, the hybrid controller determines the torque to be demanded from the electric machines and the engine to meet the total traction demand on the road and to minimize fuel consumption. Local constraints (physical limits on the speed and torque required from the electric machine and the power required from the battery) and global constraints (limits on the range of the available *SoC*) must be considered at each step, where physical and operational limits are already specified in the DDP section [93].

4.6. Artificial Neural Network (ANN)-Based Energy Management System

The mathematical modeling of the learning process was first developed in 1943 by Warren McCulloch, a neurologist, and Walter Pitts, a mathematician [95]. The ANN-based learning approach is modeled by connecting artificial neural cells in layers and aims to use the human brain's ability to learn and make decisions very quickly under different conditions to solve complex problems using simplified models [2,3,96]. ANN is ideal for developing predictive models in the presence of nonlinear relationships between inputs and outputs in large datasets and uses machine learning techniques to develop an adaptive and data-driven energy management system by capturing complex relationships between input variables and output control actions to predict the optimal energy management policy from historical driving data [3,6,11,20,34,79,81,96–98].

In the real world, ANN models trained with vehicle driving data can be used in control system modeling to determine optimal powertrain control settings in HEVs, creating networks that can predict fuel consumption for any given driving cycle, leading to improved fuel efficiency for any given driving cycle in real-time as they require minimal computing resources [3]. The performance of the ANN can be evaluated using various metrics such as fuel consumption, energy efficiency, or system performance [99].

Supervised learning and backward propagation architecture is the most widely used learning method in ANNs [96]. In this architecture, the output of the neurons in this structure depends not only on the current input values but also on the previous input values [95–97]. This algorithm minimizes the error by backpropagating the amount of error in the output of the network and calculating the effect of each weight and bias value of each neuron on the error using optimization algorithms [100–102]. In the training process, the weights and bias values, which represent the relationship between the network's input and output, are iteratively optimized according to the error value so that the network's predictions become closer to the real data and the network learns the relationship between input and output. This iterative process continues until the network converges on a satisfactory solution [101–103].

The ANN structure consists of three different layers. The input layer is the first layer that provides external data to the network and contains the neurons that receive the inputs of the data set [102,104]. The output layer produces the final predictions based on the processed input data, which contains the neurons that transmit the outputs from

the hidden layers [3,101,104]. Hidden layers are responsible for processing the input data and extracting relevant features, and the number of hidden layers and the number of neurons in each layer can vary depending on the complexity of the problem and the desired level of accuracy [96,105,106]. Neural networks learn the properties of the data and make predictions through the connections between these layers and the activation functions of the neurons [96,103]. Activation functions are applied to the outputs of each neuron in the hidden layers to give the network nonlinearity and to convert the weighted sum of a neuron's inputs into an output signal, which is then presented as input to the next layer [9,107]. The training of neural networks starts with initially randomly assigned weights and bias values and is updated to minimize the amount of error [3,101].

As shown in Figure 14, n data are entered into a cell (x_n data entries). The input data are multiplied by the weights to sum all the data and then the bias is added, resulting in a net bias. The net input is passed through the activation function and a data output is obtained [95].

$$n = \sum_{i=1}^{p} x_i \times w_i + b_j \tag{64}$$

where n is the output of the neuron, P is the number of input elements, x_i is the input value, w_i is the weight of the input value, and b_j is the bias value.

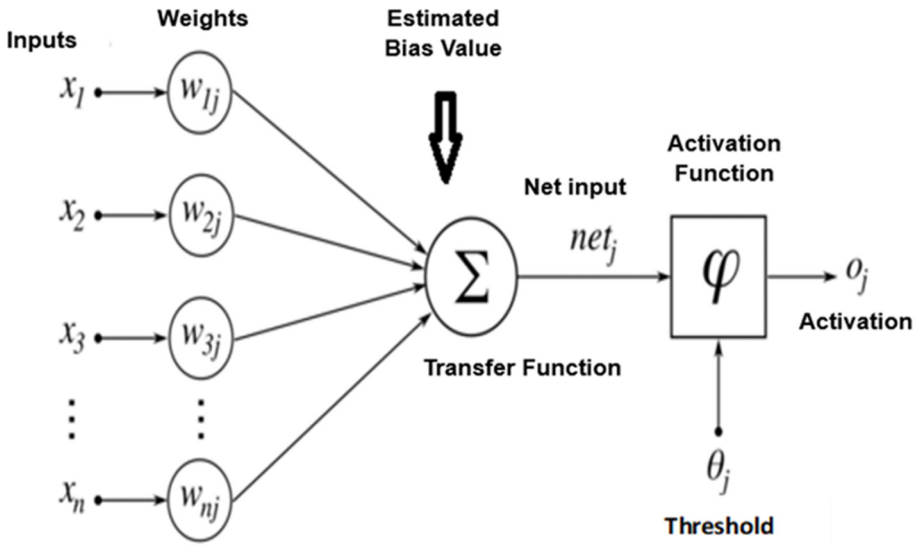

Figure 14. General structure of feedback neural networks [95].

The performance of the neural network is evaluated by calculating the correlation coefficient (R), and the mean square error (MSE) at each training iteration is expressed by the following formulation [3,96,97]. The training process tries to maximize the R-value and minimize the MSE. Weights and biases are developed using backpropagation algorithms in an iterative process and each iteration builds on the previous network by changing the weights and biases to optimize the MSE and R value [3]. The $R(a,p)$ is a measure of how well the predictions are linearly correlated with the measurements [3].

$$R(a,p) = \frac{E \times [(a-u_a) \times (p-u_p)]}{E \times \sqrt{(a-u_a)^2 \times (p-u_p)^2}} \tag{65}$$

$$MSE = \frac{1}{n}\sum_{i=1}^{n} (p_i - a_i)^2 \tag{66}$$

where p_i: targeted output value; a_i: the value obtained from the output of the network; E is the expected value; u_a and u_p are the mean values of measured and predicted output sets; and n is the number of values.

The performance of the trained networks is evaluated by calculating the percentage error in the measured and predicted FE over the entire cycle as follows.

$$\%Error = \frac{\sum_{i=1}^{n} measured_i - \sum_{i=1}^{n} predicted_i}{\sum_{i=1}^{n} measured_i} \times 100 \quad (67)$$

The sign of the error is calculated to indicate whether a model is above or below the prediction [3]. If the error value sometimes increases during training, this is usually an indication of getting away from the solution, and training stops when the validation error increases repeatedly for certain number of iterations [96]. The learning rate is a measure of the size of the step towards the minimum of a loss function or the size of the change in weight at each iteration [108]. In the histogram, the highest error density is the smallest range of data from all errors and is an indication of the performance of the ANN. If the ANN is not trained on many epochs, no significant overfitting is expected in the epoch with the best validation performance [108]. The validation phase is a critical process that involves the identification and reduction of bias in the training data and evaluation of the system's accuracy, while the testing phase is where test data are provided to each of the trained models to verify the best prediction [108].

4.6.1. Artificial Neural Network (ANN) Training Method

Levenberg–Marquardt, Bayesian Regularization, and Scaled Conjugate Gradient methods are optimization algorithms used for different purposes in training artificial neural networks. The Levenberg–Marquardt method is one of the most widely used optimization algorithms for ANN training and uses a combination of Gauss–Newton and gradient descent algorithms [97,109]. It is known for fast convergence and stability, as it is not affected by the slow convergence problem [96,110]. This method is usually used for smaller-scale problems and may not be suitable for large data sets [110,111]. Bayesian regularization is a statistical approach and uses the principles of Bayes' theorem to optimize parameters by considering the estimation uncertainty along with the estimation of the weights and bias values [112]. It offers several advantages such as improved generalization ability, reduced overfitting, and faster convergence, and it also helps to reduce the effects of noise and uncertainty [113]. The SCG method uses an iterative approach to update the weights faster and more efficiently since it uses adaptive learning rate parameters [109,114,115]. The SCG method follows the weight change with a scaling factor by using a momentum term and memory in weight updates to ensure faster convergences [114,115]. It is known for its robustness, fast convergence, efficient memory utilization, the ability to handle large-scale problems, and the ability to handle incomplete data sets [114,116].

4.6.2. Artificial Neural Network (ANN)-Based Energy Management System Design

The training of ANNs is performed on a training set, which consists of input data and target outputs [103]. The first step is the specification of the architecture of the neural network, which defines the structural properties of the network such as the number of layers, the number of neurons in each layer, and the arrangement of connections [97,117]. In the data preparation phase, the data set to be used for training is organized [97]. The data set to be used is divided into two: training data to enable the network to learn and validation data to evaluate the performance of the network [103].

The ANN-based control algorithm designed for the energy management system of hybrid electric vehicles has the following input parameters: transmission input torque, vehicle speed, battery power, and *SoC*; and based on their characteristics, a machine learning platform is designed whose only output is the hybrid driving mode, since there are five different operating modes in the charge-sustaining mode to meet the power demand [15]. The transmission input axle torque has a direct effect on the power demand and is a

necessary parameter for the selection of the hybrid driving mode, since the driving modes are primarily designed for different axle torque levels. Vehicle speed is an important parameter as it determines the kinematic constraints and vehicle kinetic energy associated with the hybrid driving mode, with higher modes associated with higher vehicle kinetic energy as more energy is delivered into the vehicle as the driving mode moves towards HERM. In sustained charge (CS) mode, where the *SoC* is relatively low, the *SoC* level influences the operating mode. Lower *SoC* levels are directly related to inefficient battery operating ranges, so modes that use more engine torque should be selected as the *SoC* drops in the CS mode. As battery performance is linked to total power demand, it is useful to distinguish between the EV1 and EV2 modes and to include the effect of regenerative braking [15]. The number of neurons used to train the artificial neural network models did not affect its performance significantly, except for certain ranges, and that is why a medium number of 10 neurons in the hidden layer was used with four inputs and one output [3]. Then, the MATLAB Neural Network Fitting Tool was used to create, train, and validate the ANN architecture as shown in Figure 15.

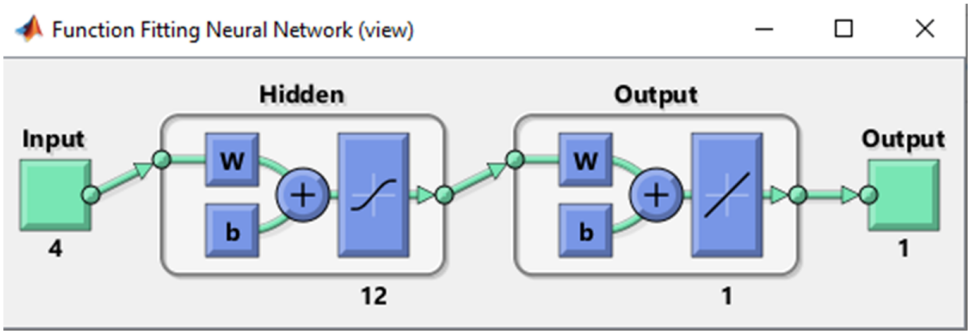

Figure 15. ANN structure development via MATLAB.

Realistic system simulations have been performed by using the rule-based and optimization-based energy management algorithms such as DDP and PMP in critical low-*SoC* (15–22%) regions for both the charge-depleting (CD) mode, which aims to use the maximum possible battery power to complete defined cycle with a minimum possible final *SoC*, and the charge-sustaining (CS) mode, which aims to keep a similar initial *SoC* level at the end of each driving cycle. Based on the simulation results obtained from the DDP and PMP optimization methods in both CD and CS mode operations, with the combination of defined driving cycles (UDDS, WLTC, NEDC, HWFET, FTP75, and JC08) at a critical low-SOC region (15–22%), different artificial neural network system structures were developed and trained by using the Levenberg–Marquardt, Bayesian Regularization, and Scaled Conjugate Gradient optimization methods. To obtain an ANN-based energy management system, 70% of the simulation data were used to train the system, 15% were used for validation, and 15% for testing. In this way, different ANN structures trained with offline simulation data were compared with each other, and the precision and accuracy in modeling were revealed.

When analyzing the best-validated system performance of designed ANN structures in terms of mean square errors (MSEs) as shown in Figure 16, which indicate how small the mean square error is when compared with the measurement, the BR and LM methods had a lower mean square error value than the SCG methods. Also, the PMP training result parameters have a slightly lower mean square error value than the DDP training results as shown in Figure 16.

Based on PMP-CS simulation data training results, the BR method showed the best validation performance in terms of MSE at around 0.39189 at epoch 1000 and the LM method was around 0.386 at epoch 296, although the SCG method was around 0.56355 at epoch 1000. Based on DDP-CS simulation data training results, the BR method showed the best validation performance in terms of MSE at around 0.4695 at epoch 826 and the LM

method was around 0.47137 at epoch 667, although the SCG method was around 0.60457 at epoch 1000.

Based on PMP-CD simulation data training results, the BR method showed the best validation performance in terms of MSE at around 0.38795 at epoch 1000 and the LM method was around 0.3698 at epoch 230, although the SCG method was around 0.75638 at epoch 419. Based on DDP-CD simulation data training results, the BR method showed the best validation performance in terms of MSE at around 0.45203 at epoch 666 and the LM method was around 0.45511 at epoch 299, although the SCG method was around 0.57412 at epoch 1000.

When analyzing the correlation coefficient (R) for regression results as shown in Figure 17, which indicate how well the predictions are linearly correlated with the measurement, the BR and LM methods had a higher correlation rate than the SCG methods. Also, the PMP training regression result parameters are slightly higher than the DDP training regression results as shown in Figure 16.

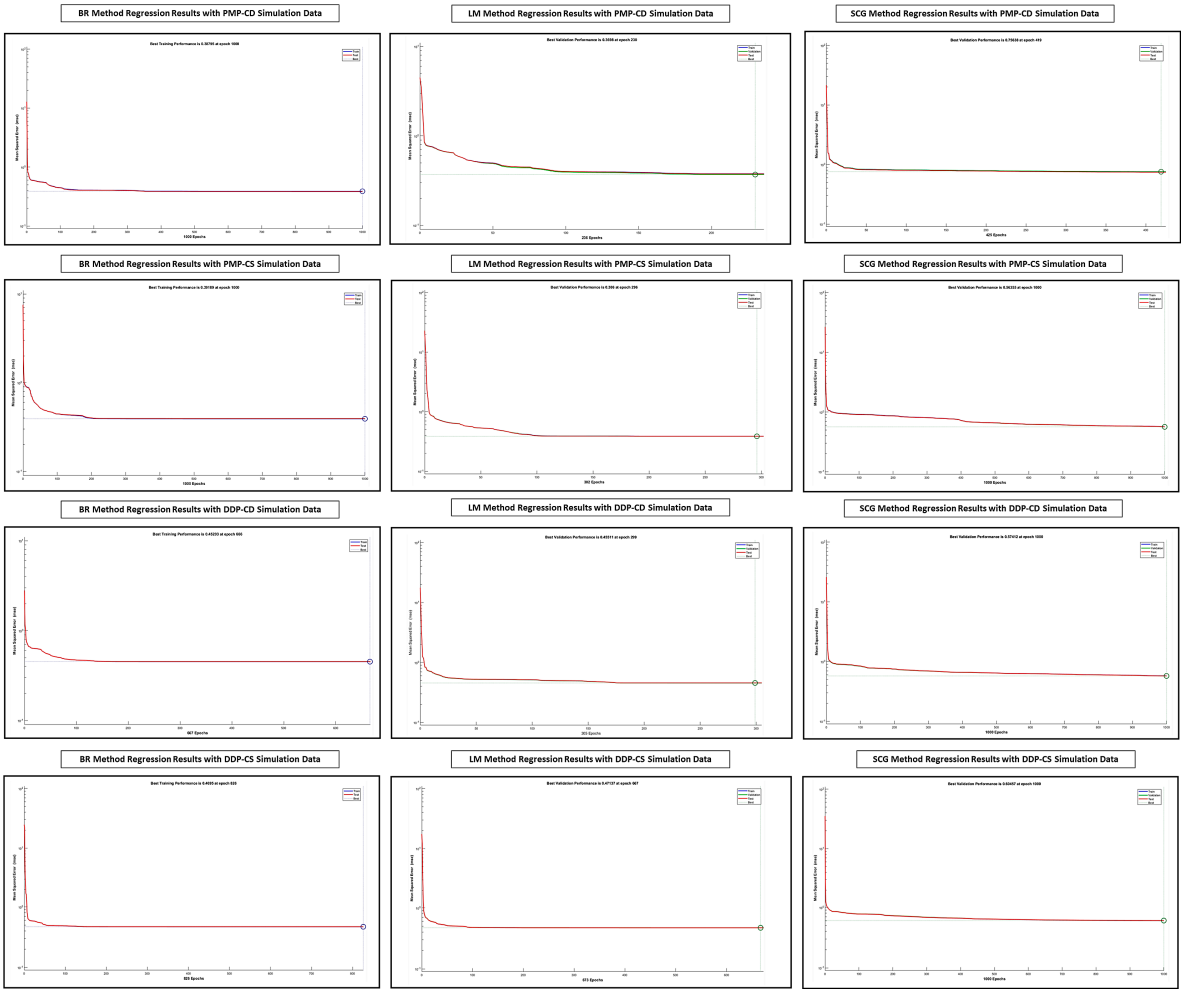

Figure 16. ANN mean square error (MSE) results with DDP and PMP CD/CS simulation data.

Based on the PMP-CS simulation data training results, the BR and LM methods showed a regression around 0.891, although the SCG method was around 0.837. Based on the DDP-CS simulation data training results, the BR and LM methods showed a regression around 0.818, although the SCG method was around 0.757.

Based on the PMP-CD simulation data training results, the BR and LM methods showed a regression around 0.874, although the SCG method was around 0.728. Based on the DDP-CD simulation data training results, the BR and LM methods showed a regression around 0.832, although the SCG method was around 0.781.

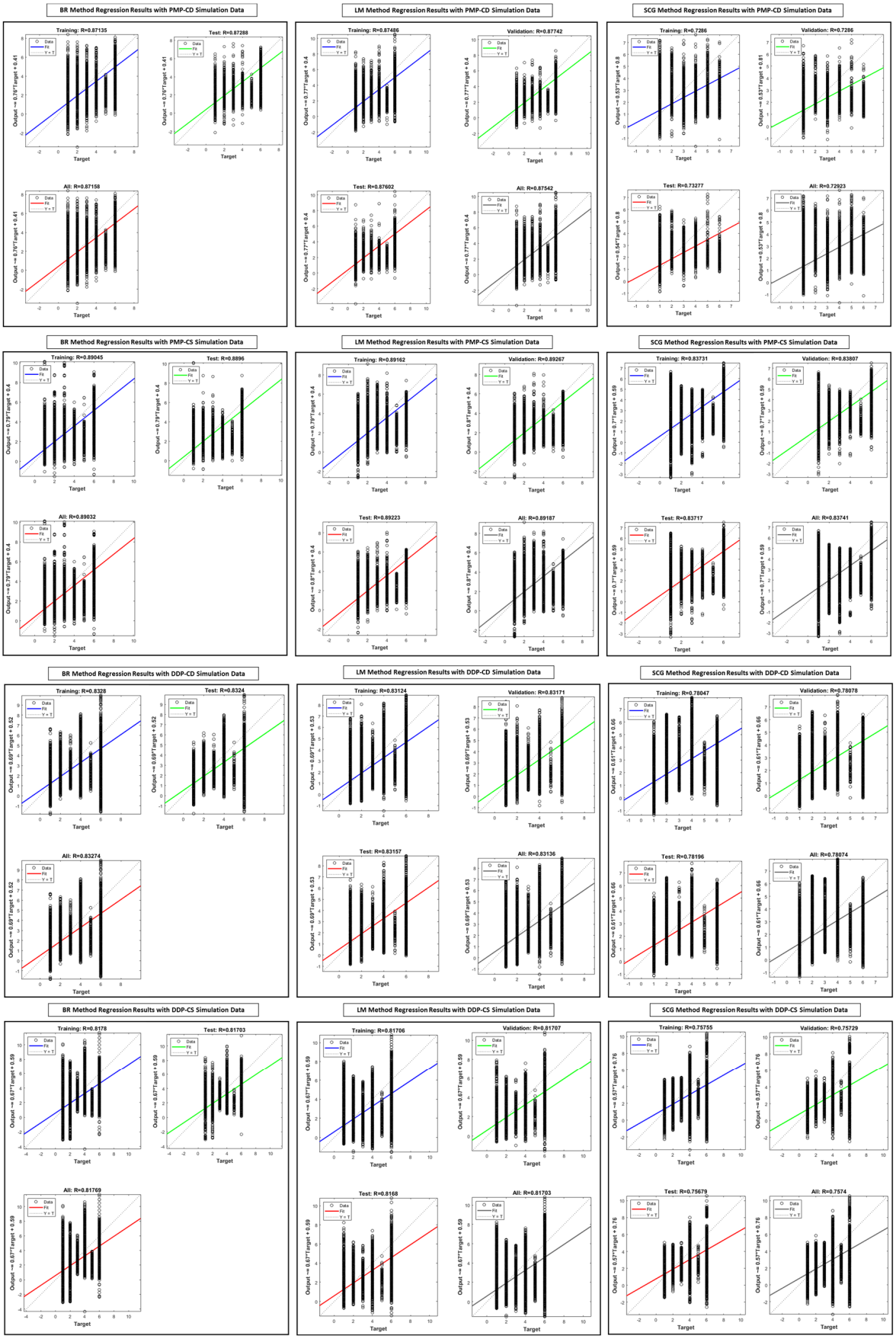

Figure 17. ANN training regression results with DDP and PMP CD/CS simulation data.

5. Discussion

In this study, the physical behaviors of the power-split hybrid electric vehicle configuration have been modeled in the Matlab/Simulink environment and validated with UDDS real vehicle chassis dynamometer data. In this way, a realistic virtual test platform has been created where different hybrid vehicle energy management system algorithms' performance will be tested and analyzed for different driving cycles and initial *SoC* levels.

Based on the FTP-75 driving cycle simulation results as shown in Figure 18, the DDP-CS method with the same initial *SoC* conditions (20%) and similar final *SoC* conditions (2.34% battery usage increased) shows a 19.19% fuel consumption reduction when compared with the rule-based method. ANN methods trained with these simulation results show an average fuel consumption reduction (DDP: 25.5%; BR: 6%; LM: 4.95%; and SCG: 2.25%), although the average battery consumption increased (DDP: 9.64%; BR: 1.37%; LM: 2.07%; and SCG: 2.11%).

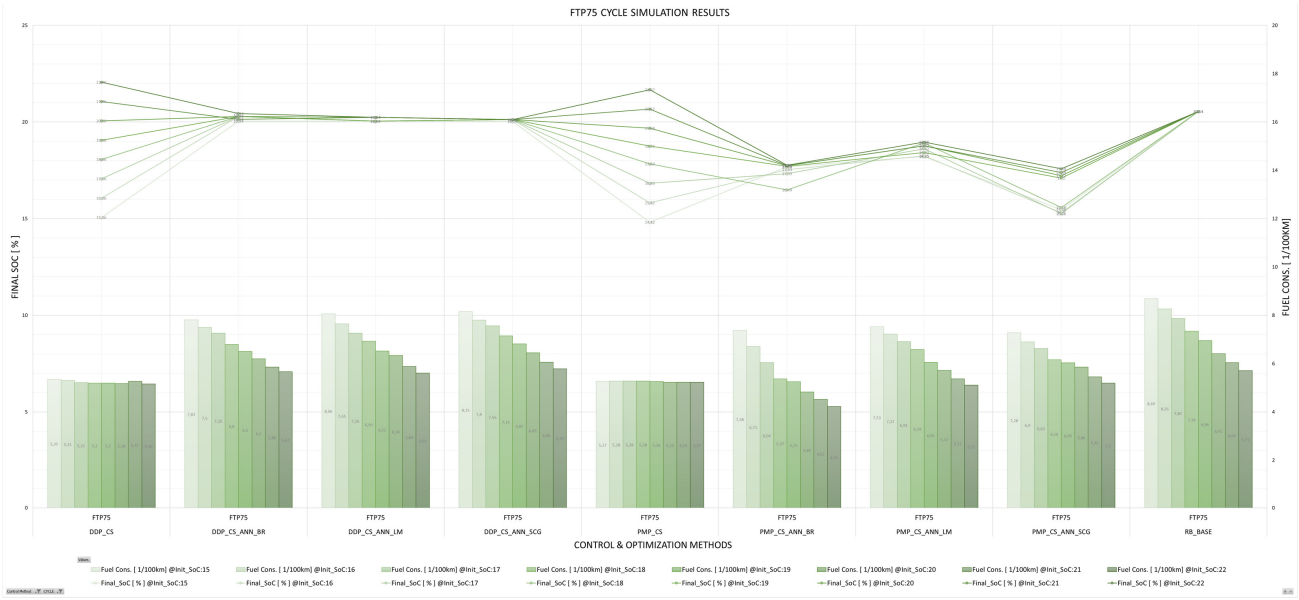

Figure 18. FTP-75 driving cycle CS mode simulation results.

The PMP-CS method, with the same initial *SoC* conditions (20%) and similar final *SoC* conditions (4.19% battery usage increased), shows an 18.41% fuel consumption reduction when compared with the rule-based method. ANN methods trained with these simulation results show an average fuel consumption reduction (PMP: 25.13%; BR: 23.03%; LM: 11.72%; and SCG: 13.16%), although average battery consumption increased (PMP: 11.11%; BR: 14.81%; LM: 9.37%; and SCG: 20.34%).

Based on the FTP-75 driving cycle simulation results as shown in Figure 19, the DDP-CD method and ANN methods trained with these simulation results show an average fuel consumption reduction (DDP: 33.26%; BR: 6.8%; LM: 0.94%; and SCG: 18.65%), although average battery consumption increased (DDP: 26.68%; BR: 7.97%; LM: 12.29%; and SCG: 17.09%).

The PMP-CD method and ANN methods trained with these simulation results show an average fuel consumption reduction (PMP: 49.83%; BR: 15.13%; LM: 28.58%; and SCG: 12.87%), although average battery consumption increased (PMP: 31.7%; BR: 9.45%; LM: 21.8%; and SCG: 10.6%).

Based on the HWFET driving cycle simulation results as shown in Figure 20, the DDP-CS method, with the same initial *SoC* conditions (22%) and nearest final *SoC* conditions (13.04 battery usage increased), show a 37.65% fuel consumption reduction when compared with the rule-based method. ANN methods trained with these simulation results show an average fuel consumption reduction (DDP: 41.26%; BR: −1.58%; LM: 4.26%;

and SCG: −20.27%), although average battery consumption increased (DDP: 21.58%; BR: −1.41%; LM: 5.87%; and SCG: −17.91%).

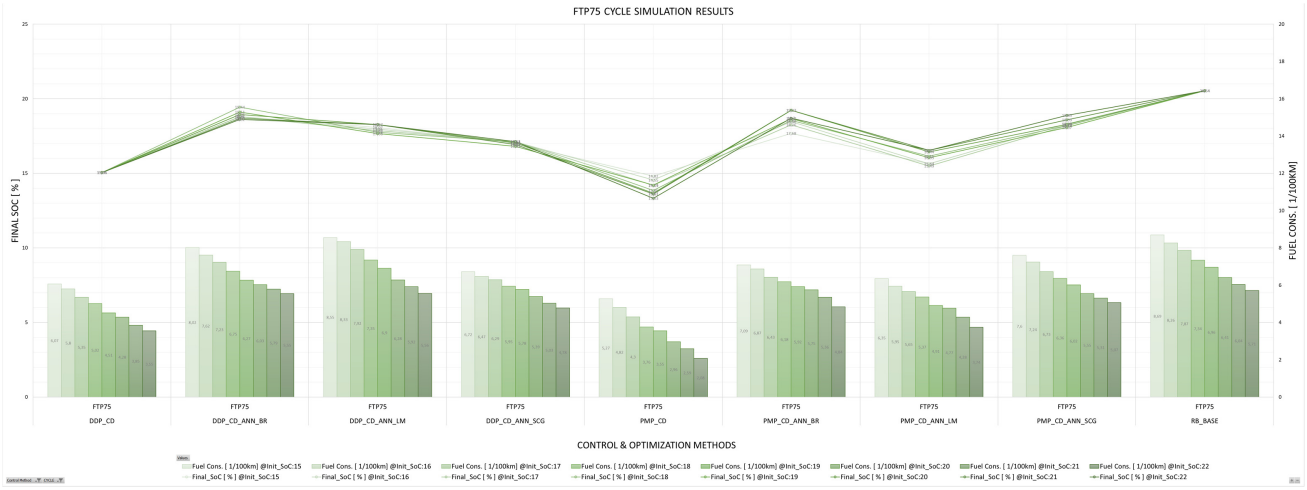

Figure 19. FTP75 driving cycle CD mode simulation results.

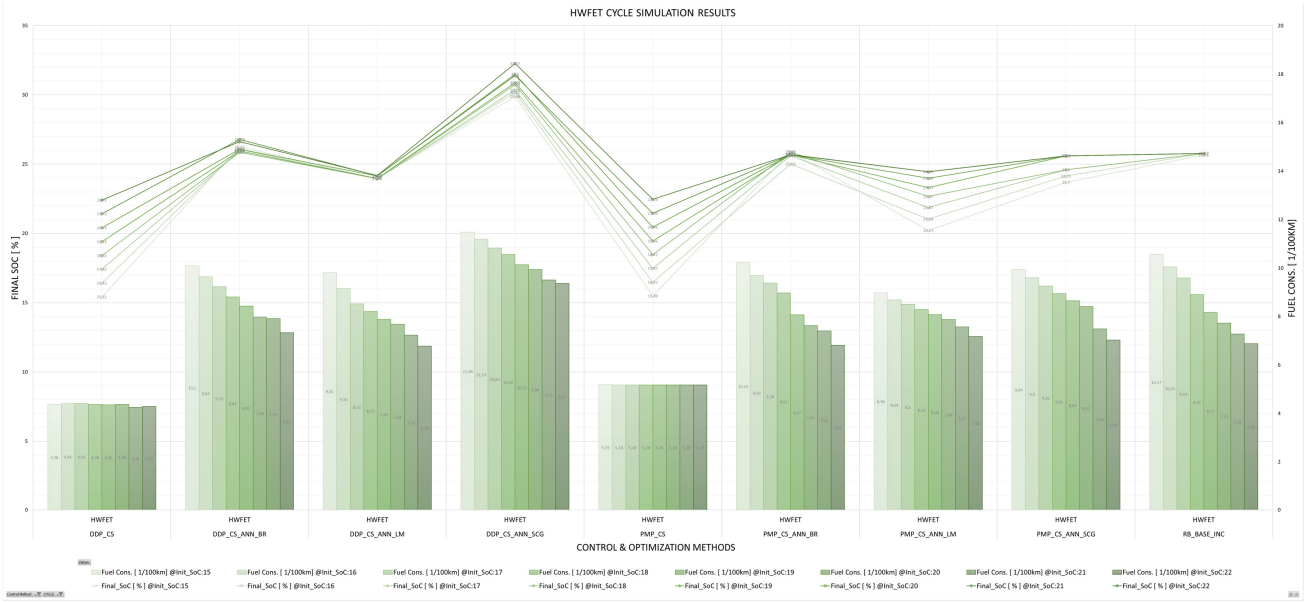

Figure 20. HWFET driving cycle CS mode simulation results.

The PMP-CS method, with the same initial *SoC* conditions (22%) and similar final *SoC* conditions (12.84 battery usage increased), shows a 24.71% fuel consumption reduction when compared with the rule-based method. ANN methods trained with these simulation results show an average fuel consumption reduction (PMP: 32.43%; BR: 0.84%; LM: 2.83%; and SCG: −1.53%), although average battery consumption increased (PMP: 21.41%; BR: 0.56%; LM: 9.03%; and SCG: 2.26%).

Based on the HWFET driving cycle simulation results as shown in Figure 21, the DDP-CD method and ANN methods trained with these simulation results show an average fuel consumption reduction (DDP: 54.55%; BR: 37.96%; LM: 13.03%; and SCG: −1.7%), although average battery consumption increased (DDP: 37.07%; BR: 33.72%; LM: 10.8%; and SCG: 0.17%).

The PMP-CD methods and ANN methods trained with these simulation results show an average fuel consumption reduction (PMP: 44.22%; BR: 4.86%; LM: −7.06%; and SCG: −4.33%), although average battery consumption increased (PMP: 31.28%; BR: 6.71%; LM: 2.58%; and SCG: −0.6%).

Figure 21. HWFET driving cycle CD mode simulation results.

Based on the JC08 driving cycle simulation results as shown in Figure 22, the DDP-CS method with the same initial *SoC* conditions (20%) and similar final *SoC* conditions (2% more battery usage), shows a 10.53% fuel consumption reduction when compared with the rule-based method. ANN methods trained with these simulation results show an average fuel consumption reduction (DDP: 14.05%; BR: 19%; LM: 4.14%; and SCG: −6.29%), although average battery consumption increased (DDP: 6.81%; BR: 10.78%; LM: 3.49%; and SCG: 1.26%).

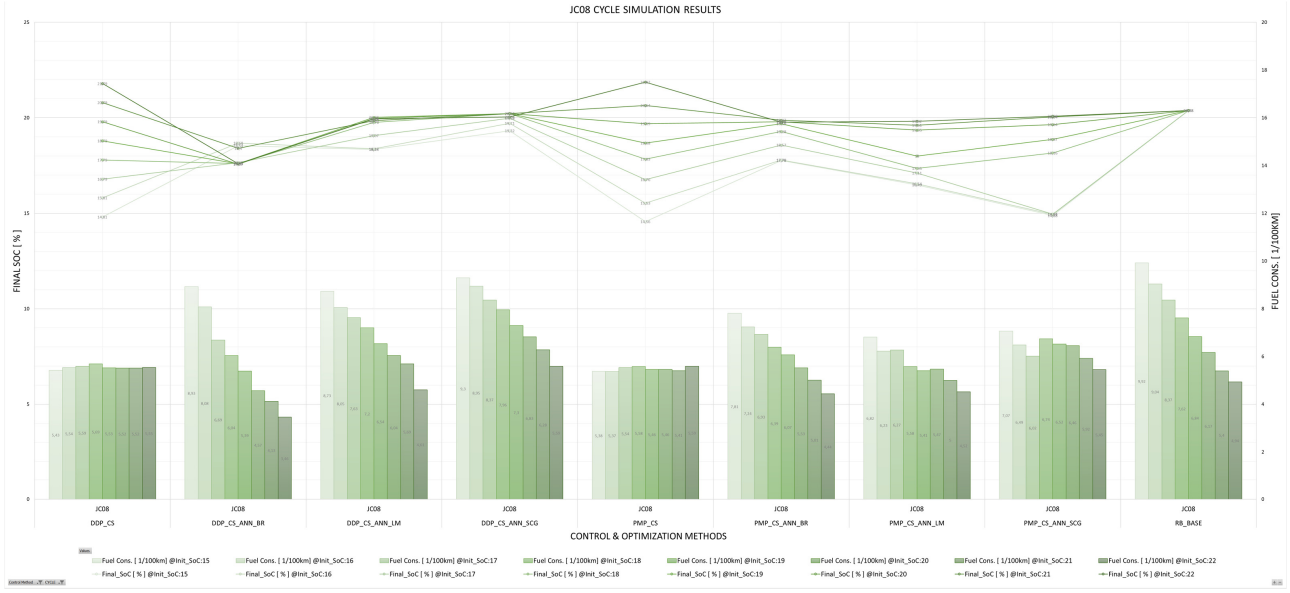

Figure 22. JC08 driving cycle CS mode simulation results.

The PMP-CS method, with the same initial *SoC* conditions (20%) and similar final *SoC* conditions (3.39% more battery usage), shows an 11.51% fuel consumption reduction when compared with the rule-based method. ANN methods trained with these simulation results show an average fuel consumption reduction (PMP: 14.94%; BR: 11.53%; LM: 16.39%; and SCG: 5.98%), although average battery consumption increased (PMP: 7.15%; BR: 4.85%; LM: 9.13%; and SCG: 9.8%).

Based on the JC08 driving cycle simulation results as shown in Figure 23, the DDP-CD method and ANN methods trained with these simulation results show an average fuel consumption reduction (DDP: 46.41%; BR: 5.71%; LM: 2.52%; and SCG: 7.61%), al-

though average battery consumption increased (DDP: 23.95%; BR: 6.34%; LM: 5.13%; and SCG: 5.52%).

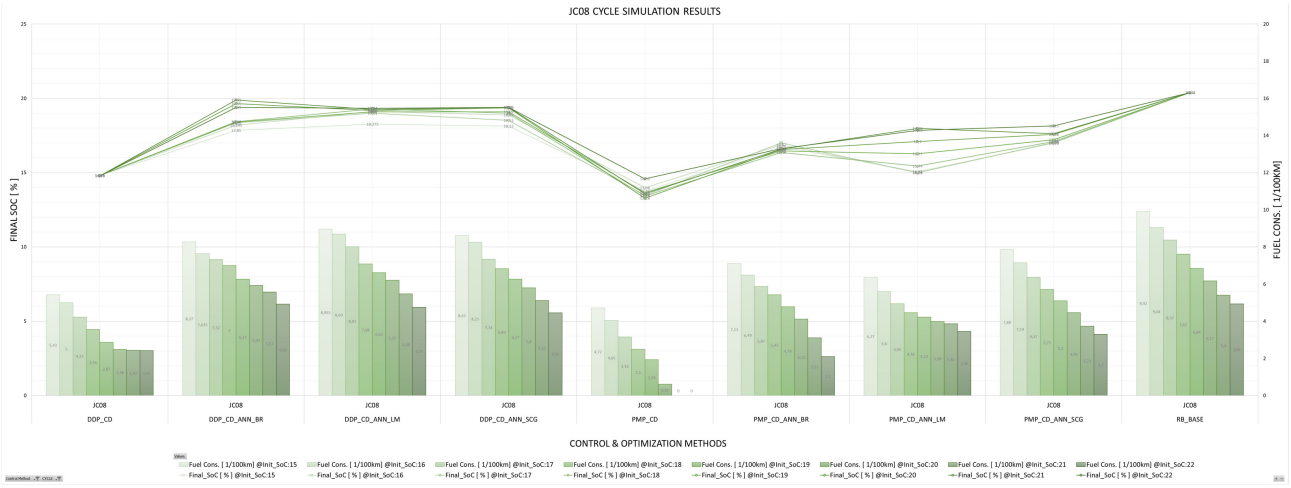

Figure 23. JC08 driving cycle CD mode simulation results.

The PMP-CD method and ANN methods trained with these simulation results show an average fuel consumption reduction (PMP: 68.32%; BR: 31.26%; LM: 31.56%; and SCG: 23.41%), although average battery consumption increased (PMP: 28.62%; BR: 16.07%; LM: 17.19%; and SCG: 12.86%).

Based on the NEDC simulation results as shown in Figure 24, the DDP-CS method, with the same initial *SoC* conditions (20%) and similar final *SoC* conditions (2.38% more battery usage), shows a 12.88% fuel consumption reduction when compared with the rule-based method. ANN methods trained with these simulation results show an average fuel consumption reduction (DDP: 14.81%; BR: −25.60%; LM: 3.89%; and SCG: −74.52%), although average battery consumption increased (DDP: 5.44%; BR: −0.21%; LM: 7.37%; and SCG: −29.65%).

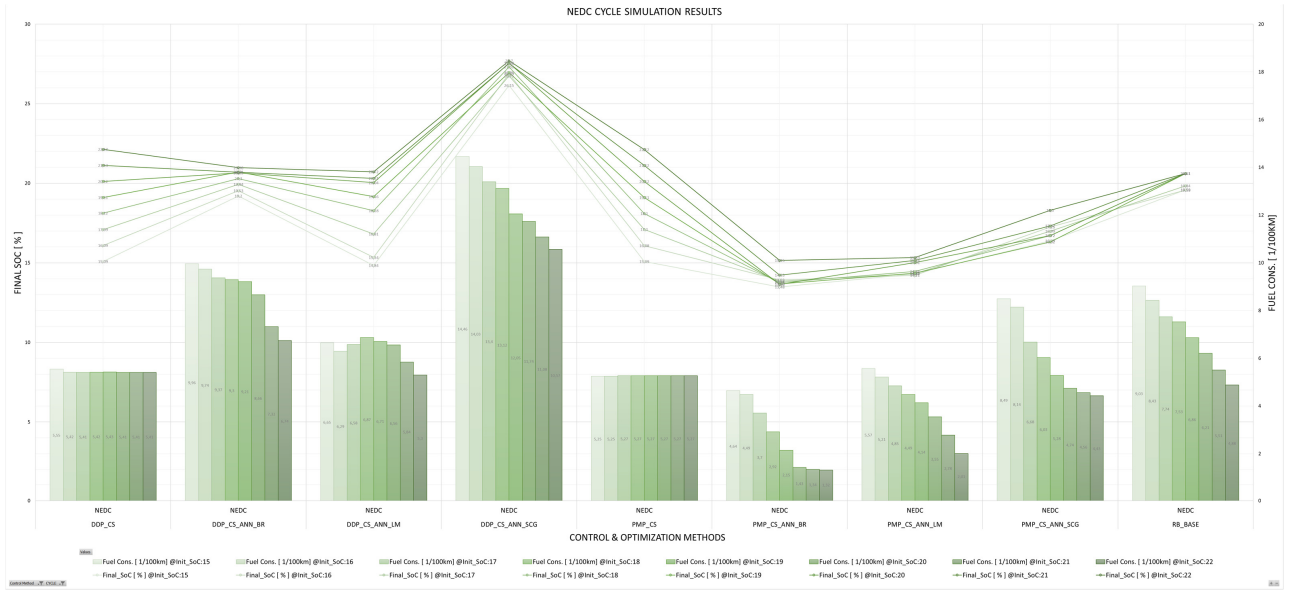

Figure 24. NEDC driving cycle CS mode simulation results.

The PMP-CS simulation results, with the same initial *SoC* conditions (20%) and similar final *SoC* conditions (2.38% more battery usage), show a 15.14% fuel consumption reduction when compared with the rule-based method. ANN methods trained with these simulation

results show an average fuel consumption reduction (PMP: 16.79%; BR: 56.8%; LM: 38.34%; and SCG: 13.78%), although battery consumption increased (PMP: 5.46%; BR: 27.15%; LM: 24.33%; and SCG: 14%).

Based on the NEDC simulation results as shown in Figure 25, the DDP-CD method and ANN method trained with these simulation results show an average fuel consumption reduction (DDP: 42.08%; BR: 52.76%; LM: 34.16%; and SCG: −33.19%), although average battery consumption increased (DDP: 22.36%; BR: 27.10%; LM: 19.5%; and SCG: −6.5%).

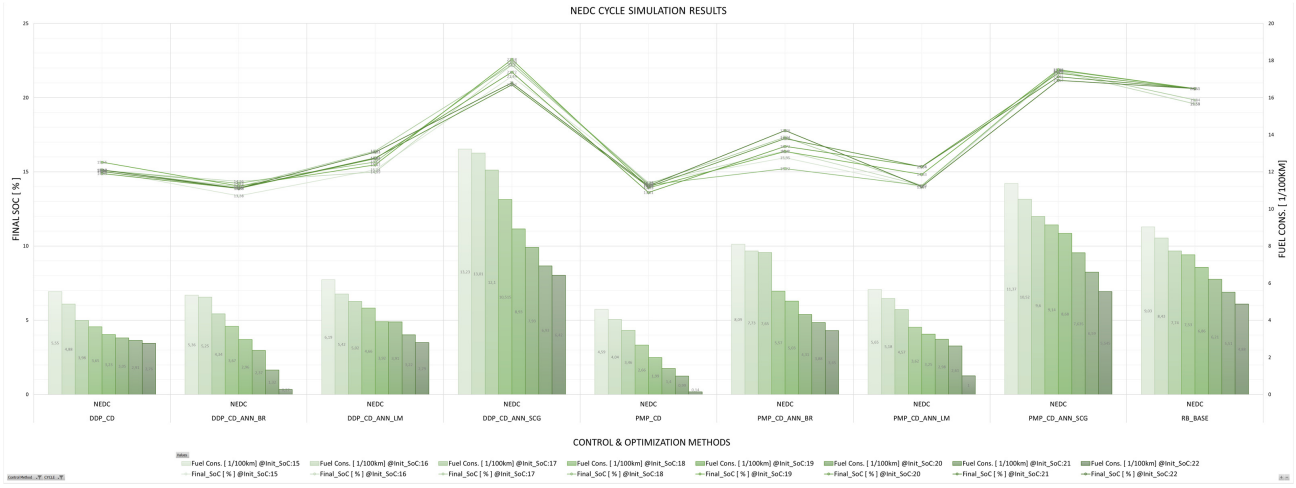

Figure 25. NEDC driving cycle CD mode simulation results.

The PMP-CD method and ANN methods trained with these simulation results show an average fuel consumption reduction (PMP: 62.46%; BR: 18.96%; LM: 46.03%; and SCG: −19.11%), although battery consumption increased (PMP: 27.19%; BR: 15.56%; LM: 25.01%; and SCG: −5.62%).

Based on the UDSS simulation results as shown in Figure 26, the DDP-CS method, with the same initial *SoC* conditions (20%) and similar final *SoC* conditions (1.19% less battery usage), shows a 13.19% fuel consumption reduction when compared with the rule-based method. ANN methods trained with these simulation results show an average fuel consumption reduction (DDP: 19.84%; BR: 1.54%; LM: 1.07%; and SCG: 1.11%), although average battery consumption increased (DDP: 2.96%; BR: −0.25%; LM: −0.1%; and SCG: 1.24%).

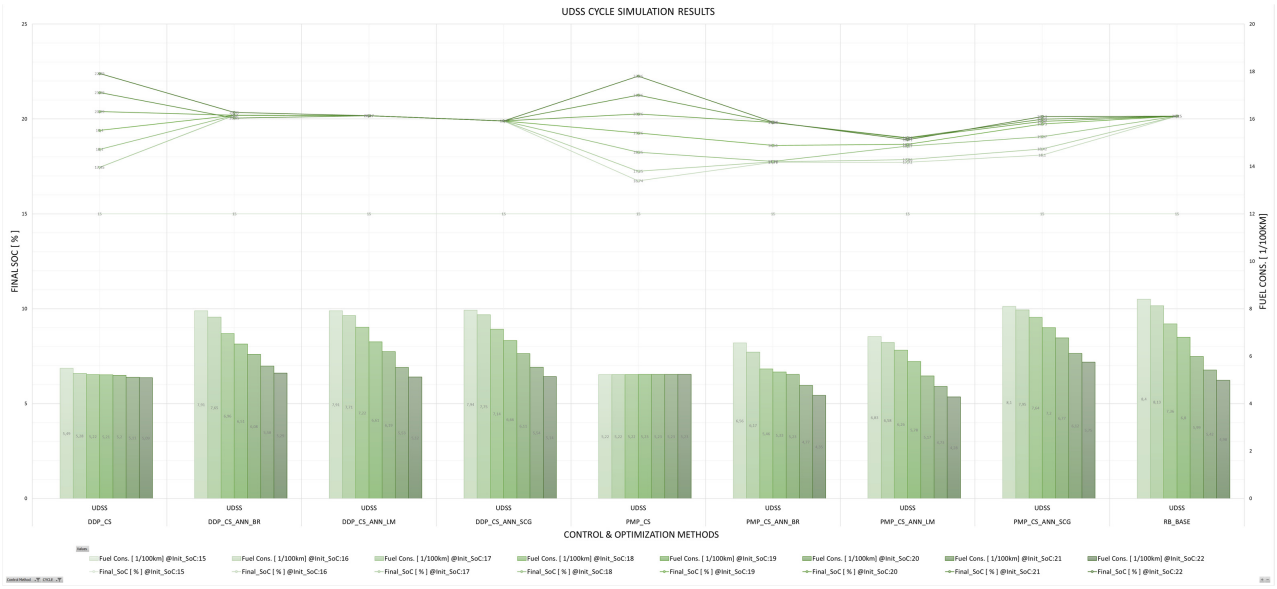

Figure 26. UDDS driving cycle CS mode simulation results.

The PMP-CS simulation results, with the same initial *SoC* conditions (20%) and similar final *SoC* conditions (0.55% less battery usage), show a 12.69% fuel consumption reduction when compared with the rule-based method. ANN methods trained with these simulation results show an average fuel consumption reduction (PMP: 19.57%; BR: 18.68%; LM: 15.45%; and SCG: −6.47%), although average battery consumption increased (PMP: 4.09%; BR: 6.91%; LM: 8.04%; and SCG: 4.07%).

Based on the UDSS simulation results as shown in Figure 27, the DDP-CD method and ANN methods trained with these simulation results show an average fuel consumption reduction (DDP: 49.89%; BR: 3.78%; LM: 0.66%; and SCG: 17.89%), although average battery consumption increased (DDP: 20.1%; BR: 1.88%; LM: 7.57%; and SCG: 10.07%).

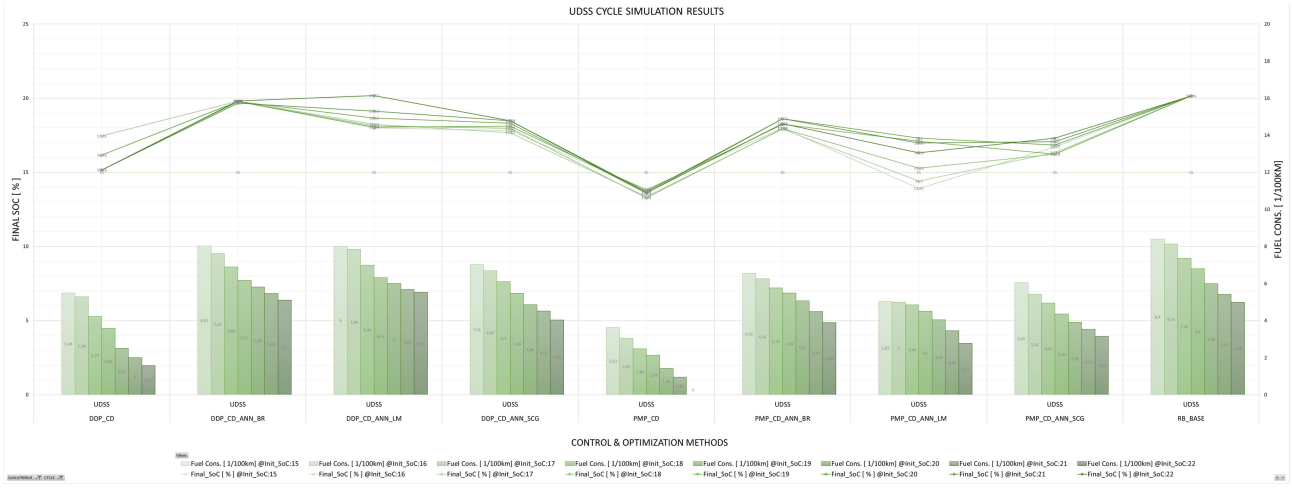

Figure 27. UDDS driving cycle CD mode simulation results.

The PMP-CD method and ANN methods trained with these simulation results show an average fuel consumption reduction (PMP: 73.24%; BR: 20.04%; LM: 37.07%; and SCG: 33.75%), although average battery consumption increased (PMP: 32.52%; BR: 9.55%; LM: 21.1%; and SCG: 17.26%).

Based on the WLTC simulation results as shown in Figure 28, the DDP-CS method, with the same initial *SoC* conditions (21%) and similar final *SoC* conditions (1.73% less battery usage), shows an 8.16% fuel consumption reduction when compared with the rule-based method. ANN methods trained with these simulation results show an average fuel consumption reduction (DDP: 14.30%; BR: −5.55%; LM: −2.55%; and SCG: −3.67%), although average battery consumption increased (DDP: 6.88%; BR: −1.13%; LM: −0.34%; and SCG: 0%).

The PMP-CS method results, with the same initial *SoC* conditions (21%) and similar final *SoC* conditions (2.4% more battery usage), show an 11.75% fuel consumption reduction when compared with the rule-based method. The ANN method trained with these simulation results shows an average fuel consumption reduction (PMP: 17.16%; BR: 21.33%; LM: 16.8%; and SCG: 19.94%), although average battery consumption increased (PMP: 10.8%; BR: 28.4%; LM: 24.17%; and SCG: 26.21%).

Based on the WLTC simulation results as shown in Figure 29, the DDP-CD method and ANN methods trained with these simulation results show an average fuel consumption reduction (DDP: 38.95%; BR: 7.3%; LM: 23.14%; and SCG: 11.1%), although average battery consumption increased (DDP: 27.8%; BR: 9.6%; LM: 34.9%; and SCG: 16.2%).

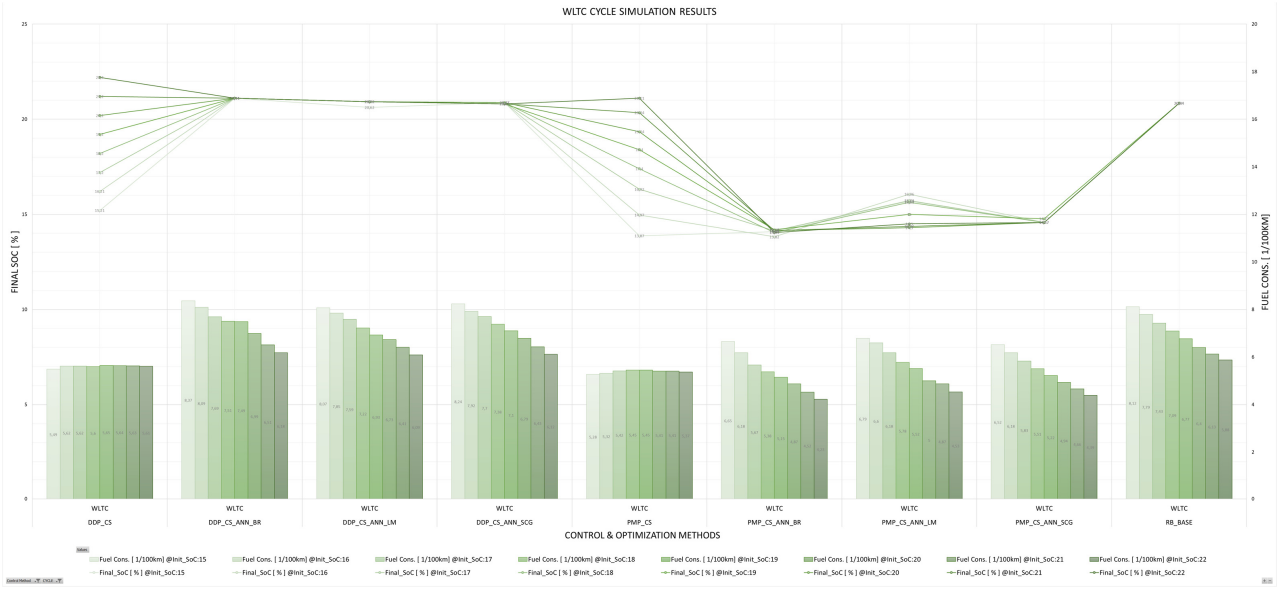

Figure 28. WLTC driving cycle CS mode simulation results.

Figure 29. WLTC driving cycle CD mode simulation results.

The PMP-CD method and ANN methods trained with these simulation results show an average fuel consumption reduction (PMP: 38.51%; BR: 23.81%; LM: 10.02%; and SCG: 8.19%), although average battery consumption increased (PMP: 30.75%; BR: 28.4%; LM: 16.27%; and SCG: 15.19%).

To summarize, in charge-sustaining (CS) mode simulation results, similar fuel consumption levels were obtained for different *SoC* levels due to same level of battery energy used in both PMP and DDP simulations, which results in lower fuel consumption compared with the rule-based controller at similar initial and final *SoC* ranges. PMP and DDP optimization algorithms show similar behaviors in CS mode in terms of fuel consumption and battery electrical energy consumption, while the engine BSFC and electric machines' efficiency are at a similar level. In charge-depleting (CD) mode simulations, much lower fuel consumption levels are obtained for different *SoC* levels in each driving cycle, due to usage of battery energy as much as possible with the lowest allowable final *SoC* range. When comparing CD simulation results with rule-based algorithms, both the DDP and PMP optimization methods have lower fuel consumption values than the rule-based controller but also more battery energy was used during simulations. Overall, PMP has lower or similar fuel consumption values than the DDP optimization method.

Overall, SCG-based training optimization methods resulted with higher fuel consumption values than LM and BR training optimization methods with similar final *SoC* ranges in most of the driving cycle results, both for CS and CD simulations as shown in Figure 18–29. CS and CD simulation results for DDP-based ANN training results showed a higher fuel consumption, while the final *SoC* values were higher than or slightly similar to the PMP-based ANN training results, except for some points in CD simulations.

Based on the DDP-based ANN training results, overall, CS-based simulations use less battery power which cause a slightly higher final *SoC* value and fuel consumption. Although, PMP-based ANN training results in CS mode show similar or reverse behavior. Based on the DDP- and PMP-based ANN training results, overall, the CS mode simulation results show a slight improvement in fuel consumption compared to the rule-based algorithm with a similar initial and final *SoC* range, although some CD mode simulation results have a lower fuel consumption due to the lower final *SoC* for the same initial *SoC* values.

6. Conclusions

To summarize, although they require intensive vehicle tests and calibration effort, rule-based controllers are a commonly used method in the automotive industry due to their lower computational loads and ability to operate in real-time. Because of the higher computational load and requirement of drive cycle information in advance, it is not possible to apply both Pontryagin's minimum principle (PMP) and discrete dynamic programming (DDP) methods in real-time applications. According to the simulation results, the best performance results were obtained by using the PMP-based optimal controller, which has the heaviest computational load. Also, the DDP method showed higher computational speed than the PMP method and gave better results than the rule-based algorithm. Finally, the artificial neural network-based algorithms, which were trained with the data obtained from PMP and DDP optimization-based methods, showed successful results with much lower computational loads, and that is why it is possible to implement them in real-time applications. As a result, ANN-based energy management structures which are optimized with Levenberg–Marquard, Bayesian Regulation, and Scaled Conjugated Gradient methods have proven their superiority by showing successful results compared to the rule-based energy management algorithm.

In conclusion, the high performance of the optimal energy management system of the artificial neural network models developed using different driving cycles and initial *SoC* levels has been proven, and analyses and comparisons were conducted according to the magnitudes affecting performance criteria such as engine fuel consumption and BSFC and electric machines' efficiency based on battery initial state of charge for various driving cycles. The proposed deep learning method also proved its ability to learn patterns and has a revolutionary potential to make an impact in the automotive industry for energy efficiency and fuel consumption reduction as well as for improvement in emissions, while it can always enhance itself by means of drive optimization data provided from different drive conditions.

Author Contributions: Conceptualization, Y.E.A. and O.A.K.; methodology, Y.E.A. and O.A.K.; validation, Y.E.A.; formal analysis and investigation, Y.E.A.; data curation, Y.E.A.; writing—original draft preparation, Y.E.A.; review and editing, O.A.K.; visualization, Y.E.A.; supervision and project administration, O.A.K. All authors have read and agreed to the published version of the manuscript.

Funding: This research received no external funding.

Data Availability Statement: Data are contained within the article.

Acknowledgments: This work is presented as part of the Ph.D. thesis work at Istanbul Technical University, Faculty of Mechanical Engineering. The authors would like to thank FEV Turkey and the ITU Automotive Department for their contributions, support, expertise, and assistance at all stages of the realization of this work.

Conflicts of Interest: The authors declare no conflicts of interest.

Abbreviations

The following abbreviations are used in this manuscript: ANNs, artificial neural networks; BR, Bayesian regularization; BSFC, break specific fuel consumption; C1, clutch 1; C2, clutch 2; CD, charge-depleting mode; CO_2, carbon dioxide; CS, charge-sustaining mode; DDP, discrete dynamic programming; ECU, electric control unit; ED, electric driving mode; EM, electric machine; EMSs, energy management systems; EPA, Environmental Protection Agency; EU, European Union; EV1, electric drive mode 1; EV2, electric drive mode 2; FC, fuel consumption; FERM, fixed gear extended range mode; FF, fuel flow; FF, fuel flow rate [g/s]; FMEP, friction mean effective pressure; FTP75, federal test procedure 75; HCU, hybrid control unit; HERM, high extended range mode; HEV, hybrid electric vehicle; HWFET, highway fuel economy driving schedule; ICE, internal combustion engine; IMEP, indicated mean effective pressure; JC08, Japanese Cycle '08; LERM, low extended range mode; LM, Levenberg–Marquardt; MEP, mean effective pressure; MGA, motor-generator A; MGB, motor-generator B; MSE, mean square error; NEDC, new European driving cycle; OC, open circuit; OCV, open circuit voltage; OWC, one-way clutch; PGS1, planetary gear set 1; PGS2, planetary gear set 2; PI, proportional integral controller; PID, proportional integral derivative controller; PMP, Pontryagin's minimum principle; RB, rule-based; SCG, scaled conjugate gradient; *SoC*, state of charge; TCU, transmission control unit; UDDS, urban dynamometer driving schedule; WLTC, worldwide harmonized light vehicles test cycle.

Appendix A

Table A1. Technical specifications of vehicles and components.

	Technical Specifications	**Unit**	**Value**
Vehicle	Vehicle Weight	Kg	1757.67
	Deceleration Factor-F0	Nm	120.55
	Deceleration Factor-F1	Nm/(km/h)	0.6006
	Deceleration Factor-F2	$Nm/(km/h)^2$	0.026775
	Wheel Diameter	m	0.32
MGA	Motor type	[-]	Ferrite Magnet
	Maximum Power	kW	48
	Maximum Torque	Nm	118
	Maximum Speed	rpm	11,000
MGB	Motor type	[-]	NdFeB Magnet
	Maximum Power	kW	87
	Maximum Torque	Nm	280
	Maximum Speed	rpm	11000
Battery	Battery Type	[-]	Lithium-Ion
	Total Energy	kWh	18.8
	Nominal Voltage	V	355
	Maximum Power	kW	120
	Battery Pack Capacity	Ah	26
	Configuration (Serial/Parallel)	[-]	(2/96)
	Battery Pack Weight	kg	183
	Battery Pack Volume	l	148
	Cooling System	[-]	Liquid

Table A1. *Cont.*

	Technical Specifications	Unit	Value
Internal Combustion Engine	Engine Volume	cm^3	1490
	Cylinder Number	[-]	4
	Diameter/Stroke Ratio	[-]	74/86.6
	Maximum Power	kW	75 @ 5600 rpm
	Maximum Torque	Nm	140 @ 4300 rpm
	Compression Ratio	[-]	12.5:1
Planetary Gear System 1	Sun/Ring Gear Ratio	[-]	0.535
	Sun/Carrier Gear Ratio	[-]	2.299
	Carrier/Ring Gear Ratio	[-]	0.233
Planetary Gear System 2	Sun/Ring Gear Ratio	[-]	0.481
	Sun/Carrier Gear Ratio	[-]	1.857
	Carrier/Ring Gear Ratio	[-]	0.259
Differential	Final Drive Ratio	[-]	2.64

References

1. Hwang, H.-Y.; Chen, J.-S. Optimized Fuel Economy Control of Power-Split Hybrid Electric Vehicle with Particle Swarm Optimization. *Energies* **2020**, *13*, 2278. [CrossRef]
2. Gautam, A.K.; Tariq, M.; Pandey, J.P.; Verma, K.S.; Urooj, S. Hybrid Sources Powered Electric Vehicle Configuration and Integrated Optimal Power Management Strategy. *IEEE Access* **2022**, *10*, 121684–121711. [CrossRef]
3. Galang, A. Predicting Hybrid Vehicle Fuel Economy and Emissions with Neural Network Models Trained with Real World Data. Master's Thesis, Colorado State University, Fort Collins, CO, USA, 2017. Available online: https://mountainscholar.org/bitstream/handle/10217/181369/Galang_colostate_0053N_14096.pdf (accessed on 12 February 2024).
4. Tribioli, L.; Onori, S. Analysis of Energy Management Strategies in Plug-in Hybrid Electric Vehicles: Application to the GM Chevrolet Volt. In Proceedings of the 013 American Control Conference, Washington, DC, USA, 17–19 June 2013. [CrossRef]
5. Yuan, Z.; Teng, L.; Fengchun, S.; Peng, H. Comparative Study of Dynamic Programming and Pontryagin's Minimum Principle on Energy Management for a Parallel Hybrid Electric Vehicle. *Energies* **2013**, *6*, 2305–2318. [CrossRef]
6. Enang, W.; Bannister, C. Modelling and Control of Hybrid Electric Vehicles (a Comprehensive Review). *Renew. Sustain. Energy Rev.* **2017**, *74*, 1210–1239. [CrossRef]
7. Surresh, K. Modelling and Analysis of Chevy Volt Gen II Hybrid Vehicle in Electric Mode. Master's Thesis, Michigan Technological University, Houghton, MI, USA, 2018. [CrossRef]
8. Muhammad, A.; Haruna, I.S. Hybrid Electric Vehicles: A Mini Overview. *J. Mod. Manuf. Syst. Technol.* **2021**, *5*, 27–36. [CrossRef]
9. Barmaki, R.; Ilkhani, M.; Salehpour, S. Investigation of energy usage and emissions on plug-in and hybrid electric vehicle. *Tech. Gaz.* **2016**, *23*, 899–906.
10. Millo, F.; Rolando, L.; Fuso, R.; Bergshoeff, E.; Shafiabady, F. Analysis of Different Energy Management Strategies for Complex Hybrid Electric Vehicles. *Comput. Aided Des. Appl.* **2014**, *11* (Suppl. S1), S1–S10. [CrossRef]
11. Singh, K.V.; Bansal, H.O.; Singh, D. A Comprehensive Review on Hybrid Electric Vehicles: Architectures and Components. *J. Mod. Transp.* **2019**, *27*, 77–107. [CrossRef]
12. Zhang, F.; Wang, L.; Coskun, S.; Pang, H.; Cui, Y.; Xi, J. Energy Management Strategies for Hybrid Electric Vehicles: Review, Classification, Comparison, and Outlook. *Energies* **2020**, *13*, 3352. [CrossRef]
13. Chan, C.C. The State of the Art of Electric, Hybrid, and Fuel Cell Vehicles. *Proc. IEEE* **2007**, *95*, 704–718. [CrossRef]
14. Benajes, J.; García, A.; Monsalve-Serrano, J.; Martínez-Boggio, S. Emissions Reduction from Passenger Cars with RCCI Plug-in Hybrid Electric Vehicle Technology. *Appl. Therm. Eng.* **2020**, *164*, 114430. [CrossRef]
15. Bhasme, S.; Hemmati, S.; Robinette, D.L.; Shahbakhti, M. Modelling of Chevy Volt Gen II Supervisory Controller in Charge Sustaining Mode. In Proceedings of the 2019 International Conference on Advanced Vehicle Powertrains, ICAVP, Hefei, China, 25–27 August 2019.
16. Liu, T.; Yu, H.; Hu, X. Robust Energy Management Strategy for a Range Extender Electric Vehicle via Genetic Algorithm. In Proceedings of the IEEE Vehicle Power Propulsion Conference (IEEE VPPC), Chicago, IL, USA, 27–30 August 2018; pp. 1–6.
17. Sharma, R.D.; Sharma, D.; Awasthi, K.; Shamsi, N.A. Power Management and Energy Optimization in Hybrid Electric Vehicle—A Review. In *Advances in Fluid and Thermal Engineering, Lecture Notes in Mechanical Engineering*; Springer: Singapore, 2019; pp. 585–594. [CrossRef]

18. Cheng, M.; Sun, L.; Buja, G.; Song, L. Advanced Electrical Machines and Machine-Based Systems for Electric and Hybrid Vehicles. *Energies* **2015**, *8*, 9541–9564. [CrossRef]
19. Zhang, X.; Eben Li, S.; Peng, H.; Sun, J. Efficient Exhaustive Search of Power-Split Hybrid Powertrains with Multiple Planetary Gears and Clutches. *J. Dyn. Syst. Meas. Control* **2015**, *137*, 121006. [CrossRef]
20. Zhang, F.; Tribioli, L. Energy-based Design of Powertrain for a Re-engineered Post-transmission Hybrid Electric Vehicle. *Energies* **2017**, *7*, 918. [CrossRef]
21. Yadav, R. Modeling and Analysis of Energy Consumption in Chevrolet Volt Gen II Hybrid Electric Vehicle. Master's Thesis, Michigan Technological University, Houghton, MI, USA, 2021. [CrossRef]
22. Zhao, J.; Odeim, F.; Chen, B.; Maiterth, J.M.; Birmes, G. FEV Simulation and Optimization Tools and Their Usage for Hybrid Powertrain Sizing. In *Der Antrieb von Morgen 2019: Diversifizierung Konsequent Vorantreiben 13. Internationale MTZ-Fachtagung Zukunftsantriebe*; Springer Vieweg: Wiesbaden, Germany, 2019; pp. 191–206. [CrossRef]
23. Morra, E.; Lenz, M.; Glados, F.; Espig, M.; Awarke, A.; Stapelbroek, M. *FEV Hybrid System Benchmarking: Synergetic Testing, Simulation and Design Assessment*; FEV Group GmbH: Aachen, Germany, 2016.
24. Zhang, X.; Li, C.-T.; Kum, D.; Peng, H. Prius^{+} and Volt^{-}: Configuration Analysis of Power-Split Hybrid Vehicles with a Single Planetary Gear. *IEEE Trans. Veh. Technol.* **2012**, *61*, 3544–3552. [CrossRef]
25. Liu, J.; Peng, H. Modeling and Control of a Power-Split Hybrid Vehicle. *IEEE Trans. Control Syst. Technol.* **2008**, *16*, 1242–1251. [CrossRef]
26. Cai, W.; Wu, X.; Zhou, M.; Liang, Y.; Wang, Y. Review and Development of Electric Motor Systems and Electric Powertrains for New Energy Vehicles. *Automot. Innov.* **2021**, *4*, 3–22. [CrossRef]
27. Kabalan, B.; Vinot, E.; Yuan, C.; Trigui, R.; Dumand, C.; Hajji, T.E. Efficiency Improvement of a Series–Parallel Hybrid Electric Powertrain by Topology Modification. *IEEE Trans. Veh. Technol.* **2019**, *68*, 11523–11531. [CrossRef]
28. Castellano, A.; Cammalleri, M. Power Losses Minimization for Optimal Operating Maps in Power-Split HEVs: A Case Study on the Chevrolet Volt. *Appl. Sci.* **2021**, *11*, 7779. [CrossRef]
29. Wu, Y.; Zhang, Y.; Li, G.; Shen, J.; Chen, Z.; Liu, Y. A Predictive Energy Management Strategy for Multi-Mode Plug-in Hybrid Electric Vehicles Based on Multi Neural Networks. *Energy* **2020**, *208*, 118366. [CrossRef]
30. Conlon, B.M.; Blohm, T.; Harpster, M.; Holmes, A.; Palardy, M.; Tarnowsky, S.; Zhou, L. The next Generation "Voltec" Extended Range EV Propulsion System. *SAE Int. J. Altern. Powertrains* **2015**, *4*, 248–259. [CrossRef]
31. Kim, N.; Choi, S.; Jeong, J.; Vijayagopal, R.; Stutenberg, K.; Rousseau, A. Vehicle Level Control Analysis for Voltec Powertrain. *World Electr. Veh. J.* **2018**, *9*, 29. [CrossRef]
32. Onori, S.; Tribioli, L. Adaptive Pontryagin's Minimum Principle Supervisory Controller Design for the Plug-in Hybrid GM Chevrolet Volt. *Appl. Energy* **2015**, *147*, 224–234. [CrossRef]
33. Bianchi, D.; Rolando, L.; Serrao, L.; Onori, S.; Rizzoni, G.; Al-Khayat, N.; Hsieh, T.-M.; Kang, P. A Rule-Based Strategy for a Series/Parallel Hybrid Electric Vehicle: An Approach Based on Dynamic Programming. In Proceedings of the ASME 2010 Dynamic Systems and Control Conference, Cambridge, MA, USA, 12–15 September 2010; Volume 1. [CrossRef]
34. Liu, Y.; Liao, Y.G.; Lai, M.-C. Fuel Economy Improvement and Emission Reduction of 48 V Mild Hybrid Electric Vehicles with P0, P1, and P2 Architectures with Lithium Battery Cell Experimental Data. *Adv. Mech. Eng.* **2021**, *13*. [CrossRef]
35. Mansour, C.J. Trip-Based Optimization Methodology for a Rule-Based Energy Management Strategy Using a Global Optimization Routine: The Case of the Prius Plug-in Hybrid Electric Vehicle. *Proc. Inst. Mech. Eng. Part D J. Automob. Eng.* **2016**, *230*, 1529–1545. [CrossRef]
36. Sciarretta, A.; Serrao, L.; Dewangan, P.C.; Tona, P.; Bergshoeff, E.N.D.; Bordons, C.; Charmpa, L.; Elbert, P.; Eriksson, L.; Hofman, T.; et al. A Control Benchmark on the Energy Management of a Plug-in Hybrid Electric Vehicle. *Control Eng. Pract.* **2014**, *29*, 287–298. [CrossRef]
37. Enang, W.; Bannister, C.; Brace, C.; Vagg, C. Modelling and Heuristic Control of a Parallel Hybrid Electric Vehicle. *Proc. Inst. Mech. Eng. Part D J. Automob. Eng.* **2015**, *229*, 1494–1513. [CrossRef]
38. Heywood, J.B. *Internal Combustion Engine Fundamentals*; McGraw-Hill Education: Singapore, 2018.
39. Stone, R. *Introduction to Internal Combustion Engines*; Palgrave Macmillan: Basingstoke, UK, 2012.
40. Pulkrabek, W.W. *Engineering Fundamentals of the Internal Combustion Engine*; Pearson: Harlow, UK, 2014.
41. Yurdaer, T.K.-E. Comparison of Energy Consumption of Different Electric Vehicle Power Systems Using Fuzzy Logic-Based Regenerative Braking. *Eng. Perspect.* **2021**, *1*, 11–21. [CrossRef]
42. Chapman, S.J. *Electric Machinery Fundamentals*, 5th ed.; McGraw-Hill: New York, NY, USA, 2012.
43. Sezer, V. Modeling, and Optimal Power Management of a Parallel Hybrid Electric Vehicle. Master's Thesis, Istanbul Technical University, Institute of Science and Technology, Istanbul, Turkey, 2008.
44. Arnaudov, K.; Karaivanov, D.P. *Planetary Gear Trains*; CRC Press: Boca Raton, FL, USA, 2019.
45. Miri, I.; Fotouhi, A.; Ewin, N. Electric Vehicle Energy Consumption Modelling and Estimation—A Case Study. *Int. J. Energy Res.* **2020**, *45*, 501–520. [CrossRef]
46. Jiang, J.; Zhang, C. *Fundamentals and Applications of Lithium-Ion Batteries in Electric Drive Vehicles*; John Wiley & Sons: Hoboken, NJ, USA, 2015. [CrossRef]
47. Ali, A.; Kamel, H.; Sharaf, A.; Hegazy, S. Modeling and simulation of hybrid electric vehicles. *Int. Conf. Appl. Mech. Mech. Eng.* **2014**, *16*, 1–12. [CrossRef]

48. Schramm, D.; Hiller, M.; Bardini, R. *VEHICLE DYNAMICS: Modeling and Simulation*; Springer: Berlin/Heidelberg, Germany, 2019.
49. Gillespie, T.D. *Fundamentals of Vehicle Dynamics*; SAE International: Warrendale, PA, USA, 2021.
50. Felix, R.; Economou, J.T.; Knowles, K. *Modelling and Simulation of a Fuel Cell Powered Medium Duty Vehicle Platform*; Elsevier: Amsterdam, The Netherlands, 2012; pp. 215–223. [CrossRef]
51. Feng, L.; Liu, W.; Chen, B. Driving Pattern Recognition for Adaptive Hybrid Vehicle Control. *SAE Int. J. Altern. Powertrains* **2012**, *1*, 169–179. [CrossRef]
52. Lei, Z.; Cheng, D.; Liu, Y.; Qin, D.; Zhang, Y.; Xie, Q. A Dynamic Control Strategy for Hybrid Electric Vehicles Based on Parameter Optimization for Multiple Driving Cycles and Driving Pattern Recognition. *Energies* **2017**, *10*, 54. [CrossRef]
53. Zhang, Q.; Fu, X. A Neural Network Fuzzy Energy Management Strategy for Hybrid Electric Vehicles Based on Driving Cycle Recognition. *Appl. Sci.* **2020**, *10*, 696. [CrossRef]
54. Divakarla, K.P.; Emadi, A.; Razavi, S.N. Journey Mapping—A New Approach for Defining Automotive Drive Cycles. *IEEE Trans. Ind. Appl.* **2016**, *52*, 5121–5129. [CrossRef]
55. Armenta-Déu, C.; Cattin, E. Real Driving Range in Electric Vehicles: Influence on Fuel Consumption and Carbon Emissions. *World Electr. Veh. J.* **2021**, *12*, 166. [CrossRef]
56. Liu, H.; Chen, F.; Tong, Y.; Wang, Z.; Yu, X.; Huang, R. Impacts of Driving Conditions on EV Battery Pack Life Cycle. *World Electr. Veh. J.* **2020**, *11*, 17. [CrossRef]
57. Huang, Y.; Surawski, N.C.; Organ, B.; Zhou, J.L.; Tang, O.H.H.; Chan, E.F.C. Fuel Consumption and Emissions Performance under Real Driving: Comparison between Hybrid and Conventional Vehicles. *Sci. Total Environ.* **2019**, *659*, 275–282. [CrossRef] [PubMed]
58. Awadallah, M.; Tawadros, P.; Walker, P.; Zhang, N. Impact of Low and High Congestion Traffic Patterns on a Mild-HEV Performance. *SAE Tech. Pap.* **2017**. [CrossRef]
59. Degraeuwe, B.; Weiss, M. Does the New European Driving Cycle (NEDC) Really Fail to Capture the NOX Emissions of Diesel Cars in Europe? *Environ. Pollut.* **2017**, *222*, 234–241. [CrossRef]
60. Sulaiman, N.; Hannan, M.A.; Mohamed, A.; Majlan, E.H.; Wan Daud, W.R. A Review on Energy Management System for Fuel Cell Hybrid Electric Vehicle: Issues and Challenges. *Renew. Sustain. Energy Rev.* **2015**, *52*, 802–814. [CrossRef]
61. Kaya, T.; Kutlar, O.A.; Taskiran, O.O. Evaluation of the Effects of Biodiesel on Emissions and Performance by Comparing the Results of the New European Drive Cycle and Worldwide Harmonized Light Vehicles Test Cycle. *Energies* **2018**, *11*, 2814. [CrossRef]
62. Lee, H.; Lee, K. Comparative Evaluation of the Effect of Vehicle Parameters on Fuel Consumption under NEDC and WLTP. *Energies* **2020**, *13*, 4245. [CrossRef]
63. Giakoumis, E.G.; Zachiotis, A.T. Investigation of a Diesel-Engined Vehicle's Performance and Emissions during the WLTC Driving Cycle—Comparison with the NEDC. *Energies* **2017**, *10*, 240. [CrossRef]
64. Yang, S.; Xie, H.; Chen, F.; Liu, J.; Feng, S.; Zhang, J. Research on Energy Management Strategy of Hybrid Electric Vehicles Based on Hierarchical Control in the Connected Environment. In Proceedings of the Applied Energy Symposium: MIT A + B (MITAB), Cambridge, MA, USA, 12–14 August 2020. [CrossRef]
65. Lin, X.; Wang, Z.; Wu, J. Energy Management Strategy Based on Velocity Prediction Using Back Propagation Neural Network for a Plug-in Fuel Cell Electric Vehicle. *Int. J. Energy Res.* **2021**, *45*, 2629–2643. [CrossRef]
66. Serrao, L.; Onori, S.; Rizzoni, G. A Comparative Analysis of Energy Management Strategies for Hybrid Electric Vehicles. *J. Dyn. Syst. Meas. Control* **2011**, *133*, 031012. [CrossRef]
67. Opila, D.F.; Wang, X.; McGee, R.; Gillespie, R.B.; Cook, J.A.; Grizzle, J.W. An Energy Management Controller to Optimally Trade off Fuel Economy and Drivability for Hybrid Vehicles. *IEEE Trans. Control Syst. Technol.* **2012**, *20*, 1490–1505. [CrossRef]
68. Panday, A.; Bansal, H.O. A Review of Optimal Energy Management Strategies for Hybrid Electric Vehicle. *Int. J. Veh. Technol.* **2014**, *2014*, 160510. [CrossRef]
69. Benajes, J.; García, A.; Monsalve-Serrano, J.; Martínez-Boggio, S. Optimization of the Parallel and Mild Hybrid Vehicle Platforms Operating under Conventional and Advanced Combustion Modes. *Energy Convers. Manag.* **2019**, *190*, 73–90. [CrossRef]
70. Qi, X.; Wu, G.; Boriboonsomsin, K.; Barth, M.J. Development and Evaluation of an Evolutionary Algorithm-Based OnLine Energy Management System for Plug-in Hybrid Electric Vehicles. *IEEE Trans. Intell. Transp. Syst.* **2017**, *18*, 2181–2191. [CrossRef]
71. Zhou, Y.; Wang, R.; Ding, R. Energy Optimization for Intelligent Hybrid Electric Vehicles Based on Hybrid System Approach in a Car-Following Process. *Optim. Control Appl. Methods* **2022**, *43*, 1020–1046. [CrossRef]
72. Sorlei, I.; Bizon, N.; Thounthong, P.; Varlam, M.; Raboaca, M.S.; Raceanu, M. Fuel Cell Electric Vehicles—a Brief Review of Current Topologies and Energy Management Strategies. *Energies* **2021**, *1*, 252. [CrossRef]
73. Li, J.; Zhou, Q.; Williams, H.; Xu, H. Back-To-Back Competitive Learning Mechanism for Fuzzy Logic Based Supervisory Control System of Hybrid Electric Vehicles. *IEEE Trans. Ind. Electron.* **2020**, *67*, 8900–8909. [CrossRef]
74. Aziz, A.; Tajuddin, M.; Adzman, M.; Ramli, M.; Mekhilef, S. Energy Management and Optimization of a PV/Diesel/Battery Hybrid Energy System Using a Combined Dispatch Strategy. *Sustainability* **2019**, *11*, 683. [CrossRef]
75. Dizqah, A.M.; Ballard, B.L.; Blundell, M.V.; Kanarachos, S.; Innocente, M.S. A Non-Convex Control Allocation Strategy as Energy-Efficient Torque Distributors for On-Road and Off-Road Vehicles. *Control Eng. Pract.* **2020**, *95*, 104256. [CrossRef]
76. Zhang, Y.; Zhao, H.; Huang, K.; Qiu, M.; Geng, L. Hybrid Optimization and Its Applications for Multi-Mode Plug-in Hybrid Electric Vehicle. *Proc. Inst. Mech. Eng. Part D J. Automob. Eng.* **2019**, *234*, 228–244. [CrossRef]

77. Yi, F.; Lu, D.; Wang, X.; Pan, C.; Tao, Y.; Zhou, J.; Zhao, C. Energy Management Strategy for Hybrid Energy Storage Electric Vehicles Based on Pontryagin's Minimum Principle Considering Battery Degradation. *Sustainability* **2022**, *14*, 1214. [CrossRef]
78. Karbaschian, M.A.; Söffker, D. Review and Comparison of Power Management Approaches for Hybrid Vehicles with Focus on Hydraulic Drives. *Energies* **2014**, *6*, 3512–3536. [CrossRef]
79. Han, L.; Jiao, X.; Zhang, Z. Recurrent Neural Network-Based Adaptive Energy Management Control Strategy of Plug-In Hybrid Electric Vehicles Considering Battery Aging. *Energies* **2020**, *13*, 202. [CrossRef]
80. Zou, Y.; Huang, R.; Wu, X.; Zhang, B.; Zhang, Q.; Wang, N.; Qin, T. Modeling and Energy Management Strategy Research of a Power-Split Hybrid Electric Vehicle. *Adv. Mech. Eng.* **2020**, *12*. [CrossRef]
81. Hu, X.; Liu, T.; Qi, X.; Barth, M. Reinforcement Learning for Hybrid and Plug-in Hybrid Electric Vehicle Energy Management: Recent Advances and Prospects. *IEEE Ind. Electron. Mag.* **2019**, *13*, 16–25. [CrossRef]
82. Moulik, B.; Söffker, D. Online Power Management with Embedded Offline-Optimized Parameters for a Three-Source Hybrid Powertrain with an Experimental Emulation Application. *Energies* **2016**, *9*, 439. [CrossRef]
83. Malikopoulos, A.A. Supervisory Power Management Control Algorithms for Hybrid Electric Vehicles: A Survey. *IEEE Trans. Intell. Transp. Syst.* **2014**, *15*, 1869–1885. [CrossRef]
84. Wang, W.; Cai, Z.; Liu, S. Study on Real-Time Control Based on Dynamic Programming for Plug-in Hybrid Electric Vehicles. *SAE Int. J. Elec. Veh.* **2021**, *10*, 167–176. [CrossRef]
85. Hu, J.; Wu, Z.; Li, C. Research on Energy Management Strategy of Range Extender Electric Vehicle Considering Temperature Effect under Different Heat Demands. *Int. J. Energy Res.* **2023**. [CrossRef]
86. Torreglosa, J.P.; Garcia-Triviño, P.; Vera, D.; López-García, D.A. Analyzing the Improvements of Energy Management Systems for Hybrid Electric Vehicles Using a Systematic Literature Review: How Far Are These Controls from Rule-Based Controls Used in Commercial Vehicles? *Appl. Sci.* **2020**, *10*, 8744. [CrossRef]
87. Dedes, E.K.; Hudson, D.A.; Turnock, S.R. Investigation of Diesel Hybrid Systems for Fuel Oil Reduction in Slow Speed Ocean Going Ships. *Energy* **2016**, *114*, 444–456. [CrossRef]
88. Zhang, Y.-T.; Hu, M.-B. Research on Energy Management for Hybrid Electric Vehicles in WLTP Driving Cycle. In Proceedings of the International Conference on Computer, Artificial Intelligence, and Control Engineering (CAICE 2023), Hangzhou, China, 17–19 February 2023. [CrossRef]
89. Bagwe, R.M.; Byerly, A.; dos Santos, E.C., Jr.; Ben-Miled, Z. Adaptive Rule-Based Energy Management Strategy for a Parallel HEV. *Energies* **2019**, *12*, 4472. [CrossRef]
90. Xia, C.; Zhang, C. Real-Time Optimization Power-Split Strategy for Hybrid Electric Vehicles. *Sci. China Technol. Sci.* **2016**, *59*, 814–824. [CrossRef]
91. Kim, N.; Cha, S.; Peng, H. Optimal Control of Hybrid Electric Vehicles Based on Pontryagin's Minimum Principle. *IEEE Trans. Control Syst. Technol.* **2011**, *19*, 1279–1287. [CrossRef]
92. Qiu, L.; Qian, L.; Zomorodi, H.; Pisu, P. Global Optimal Energy Management Control Strategies for Connected Four-Wheel-Drive Hybrid Electric Vehicles. *IET Intell. Transp. Syst.* **2017**, *11*, 264–272. [CrossRef]
93. Sharma, O.P. A Practical Implementation of a Near Optimal Energy Management Strategy Based on the Pontryagin's Minimum Principle in a PHEV. Master's Thesis, Ohio State University, Electrical and Computer Engineering, Columbus, OH, USA, 2012. Available online: http://rave.ohiolink.edu/etdc/view?acc_num=osu1337626310 (accessed on 13 February 2024).
94. Xie, S.; Li, H.; Xin, Z.; Liu, T.; Wei, L. A Pontryagin Minimum Principle-Based Adaptive Equivalent Consumption Minimum Strategy for a Plug-in Hybrid Electric Bus on a Fixed Route. *Energies* **2017**, *10*, 1379. [CrossRef]
95. Öztürk, K.; Şahin, M.E. Yapay sinir ağları ve yapay zekâ'ya genel bir bakış. *Takvim-I Vekayi* **2018**, *6*, 25–36.
96. Ataseven, B. Yapay sinir ağlari ile öngörü modellemesi. *Öneri* **2013**, *10*, 101–115. [CrossRef]
97. Aşkın, D.; İskender, İ.; Mamızadeh, A. Farklı Yapay Sinir Ağları Yöntemlerini Kullanarak Kuru Tip Transformatör Sargısının Termal Analizi. *J. Fac. Eng. Gazi Univ.* **2011**, *26*, 905–913.
98. Vinot, E.; Trigui, R. Optimal Energy Management of HEVs with Hybrid Storage System. *Energy Convers. Manag.* **2013**, *76*, 437–452. [CrossRef]
99. Li, K.; Jia, C.; Han, X.; He, H. A Novel Minimal-Cost Power Allocation Strategy for Fuel Cell Hybrid Buses Based on Deep Reinforcement Learning Algorithms. *Sustainability* **2023**, *15*, 7967. [CrossRef]
100. Guo, X.; Liu, T.; Tang, B.; Tang, X.; Zhang, J.; Tan, W.; Jin, S. Transfer Deep Reinforcement Learning-Enabled Energy Management Strategy for Hybrid Tracked Vehicle. *IEEE Access* **2020**, *8*, 165837–165848. [CrossRef]
101. Goodfellow, I.; Bengio, Y.; Courville, A. *Deep Learning*; MIT Press: Cambridge, MA, USA, 2016.
102. Haykin, S. *The Neural Networks a Comprehensive Foundation*; Macmillan College Publishing Company: New York, NY, USA, 1998.
103. Bishop, C.M. *Neural Networks for Pattern Recognition*; Oxford University Press: Oxford, UK, 2002.
104. Martinez, C.M.; Hu, X.; Cao, D.; Velenis, E.; Gao, B.; Wellers, M. Energy Management in Plug-in Hybrid Electric Vehicles: Recent Progress and a Connected Vehicles Perspective. *IEEE Trans. Veh. Technol.* **2017**, *66*, 4534–4549. [CrossRef]
105. Zhang, R.; Tao, J.; Zhou, H. Fuzzy Optimal Energy Management for Fuel Cell and Supercapacitor Systems Using Neural Network Based Driving Pattern Recognition. *IEEE Trans. Fuzzy Syst.* **2019**, *27*, 45–57. [CrossRef]
106. Yang, X.; Jiang, C.; Zhou, M.; Hu, H. Bi-Level Energy Management Strategy for Power-Split Plug-in Hybrid Electric Vehicles: A Reinforcement Learning Approach for Prediction and Control. *Front. Energy Res.* **2023**, *11*. [CrossRef]

107. Feldkamp, L.; Abou-Nasr, M.; Kolmanovsky, I.V. Recurrent Neural Network Training for Energy Management of a Mild Hybrid Electric Vehicle with an Ultra-Capacitor. In Proceedings of the 2009 IEEE Workshop on Computational Intelligence in Vehicles and Vehicular Systems, Nashville, TN, USA, 30 March–2 April 2009. [CrossRef]
108. Hernández, J.A.; Fernández, E.; Torres, H. Electric Vehicle NiMH Battery State of Charge Estimation Using Artificial Neural Networks of Backpropagation and Radial Basis. *World Electr. Veh. J.* **2023**, *14*, 312. [CrossRef]
109. Bishop, C.M. *Pattern Recognition and Machine Learning*; Springer: Berlin/Heidelberg, Germany, 2006.
110. Hagan, M.T.; Demuth, H.; Beale, M. *Neural Network Design*; PWS Publishing Co.: Worcester, UK, 2003.
111. Li, A.; Yuen, A.C.Y.; Wang, W.; Chen, T.B.Y.; Lai, C.S.; Yang, W.; Wu, W.; Chan, Q.N.; Kook, S.; Yeoh, G.H. Integration of Computational Fluid Dynamics and Artificial Neural Network for Optimization Design of Battery Thermal Management System. *Batteries* **2022**, *8*, 69. [CrossRef]
112. Neal, R.M. *Bayesian Learning for Neural Networks*; Springer: New York, NY, USA, 1996. [CrossRef]
113. Veerappan, P.M.; Dineshraj, V.; Elangovan, S.; Deepika, V.; Ramachandran, M.; Panchal, H.; Lamba, R.; Thangaraj, K.; Muthusamy, S. A Novel Method of Bayesian Regularization Based Solar Charging Station Employing Maximum Power Point Tracking for Electric Vehicle Applications. *Res. Sq.* **2022**. [CrossRef]
114. Møller, M.F. A Scaled Conjugate Gradient Algorithm for Fast Supervised Learning. *Neural Netw.* **1993**, *6*, 525–533. [CrossRef]
115. Hagan, M.T.; Menhaj, M.B. Training Feedforward Networks with the Marquardt Algorithm. *IEEE Trans. Neural Netw.* **1994**, *5*, 989–993. [CrossRef] [PubMed]
116. Norgaard, M. *Neural Networks for Modelling and Control of Dynamic Systems*; Springer: London, UK, 2003.
117. Nielsen, M.A. *Neural Networks and Deep Learning*; Determination Press. 2015. Available online: https://static.latexstudio.net/article/2018/0912/neuralnetworksanddeeplearning.pdf (accessed on 1 February 2024).

Disclaimer/Publisher's Note: The statements, opinions and data contained in all publications are solely those of the individual author(s) and contributor(s) and not of MDPI and/or the editor(s). MDPI and/or the editor(s) disclaim responsibility for any injury to people or property resulting from any ideas, methods, instructions or products referred to in the content.